Master of Science dissertation:

Dosimetric and geometric evaluation of MRI as the only imaging modality for the radiotherapy treatment process of localized prostate cancer

Johan Sjöberg

Supervisors:

Brian Holch Kristensen

David Sjöström

This work has been performed at the Department of oncology, Herlev university hospital, Copenhagen, Denmark

Department of Medical Radiation Physics, Clinical Sciences, Lund
Lund University, Sweden, 2010

Abstract

Introduction

MRI provides better soft tissue contrast than CT and is an invaluable tool in the radiotherapy treatment process. The gold standard today is image fusion of MRI and CT data where targets and organs-at-risk are delineated on the MRI data and the dose calculation is performed on the CT data. It is appealing to exclude CT from the process in order to reduce cost and time and to eliminate the uncertainty inherited from the image registration. Since MRI data does not contain any electron density information, this property must be assigned to the data. The purpose of this study is to evaluate the use of MRI as the only modality for the entire radiotherapy treatment process of localized prostate cancer. A study of the dosimetric consequences of MRI based dose planning and the contrast properties of novel intra-prostatic marker materials in multimodality imaging was conducted.

Materials and methods

Ten patients were selected for the dosimetry study and were both MR- and CT-scanned using routine clinical imaging parameters. 3DCRT, IMRT and VMAT plans were generated for the CT data, unit density assigned CT-data, unit density assigned MRI data and bulk density assigned MRI data. The resulting dose distributions were compared by calculating the root-mean-square values (rms) for the volumes enclosed by isodose levels 60%, 70%, 80%, 90%, 95% and 100% normalized to the prescription dose and by generating topographic maps of the percentage dose- and the absolute dose difference. DVH's were compared in order to study general tendencies in the dose distributions. The geometric distortion was studied with the help of a geometric distortion evaluation phantom provided by the vendor and the effect of using the vendors built in gradient distortion correction algorithm was studied utilizing both phantom measurements and scans of three healthy volunteers. The contrast properties of the marker implant materials was studied by inserting them in two pieces of ham followed by CT- and MRI scanning them using clinical routine protocols. Megavoltage and kilovoltage on-board imager systems capable of performing CBCT were also used to test the visibility of the markers at the linear accelerator. The best suitable marker was implanted into four volunteer patients in order to study the visibility *in vivo* with anatomical structures present.

Results

Dose discrepancies > 2 % are found mainly in clinically insignificant areas in all patients regardless if bony areas is assigned a relevant CT-number or not. The dosimetric uncertainty is however significantly reduced ($p < 0.05$) inside the target volume for the 3DCRT plans (rms at $V_{95\%}$ reduced from 1.4 ± 0.4 to 0.6 ± 0.2) but not for the VMAT plans ($p \approx 0.07$) for the bulk density assigned MRI data compared to unit density assigned MRI data (rms at $V_{95\%}$ reduced from 1.3 ± 0.6 to 1.1 ± 0.6). In contrary to the hypothesis, the dosimetric uncertainty is significantly increased ($p < 0.05$) inside the target volume for IMRT plans for bulk density assigned MRI data compared to unit density assigned MRI data (rms at $V_{95\%}$ increased from 0.8 ± 0.3 to 1.2 ± 0.4). No apparent reason for this was found, but it is believed that the chosen CT-number of 403 HU is an overestimate of the true mean for this tissue and that the fluence optimized plans are more sensitive to the choice of CT-number. Large individual differences are found when studying local percentage dose differences and are mostly prominent for the VMAT treatment technique. The gradient distortion correction algorithm reduces the geometric distortion in the MR-images but residual distortion is present. The gold/nitinol material composition for marker implants showed acceptable visibility in all imaging modalities except the on-board MV-imaging system.

Conclusion

MRI-only based radiotherapy treatment planning and setup of prostate cancer patients is feasible. Incorporating a quality assurance program in order to reduce the geometric distortion in the MR-images even further as well as assigning relevant CT-numbers to bone tissues reduces the dosimetric uncertainty, however more work is required in order to study these effects more thoroughly. The gold/nitinol material composition is recommended for use in multimodality imaging when CBCT or kV imaging is employed.

Table of Contents

Abbreviations

3DCRT – 3-dimensional conformal radiotherapy
AAA – Anisotropic analytical algorithm
BEV – Beams eye view
CBCT - Cone beam computed tomography
CT – Computed tomography
DICOM – Digital imaging and communications in medicine
DTA – Distance-to-agreement
DVH – Dose volume histogram
ETL – Echo train length
FFE – Fast field echo
FOV – Field of view
GDC – Gradient distortion correction
IGRT – Image guided radiotherapy
IMRT – Intensity modulated radiotherapy
kV - Kilo voltage
MLC – Multi leaf collimator
MRI – Magnetic resonance imaging
MV - Mega voltage
OAR – Organ at risk
PB – Pencil beam
RTP – Radiotherapy treatment planning
PTV – Planning target volume
TE – Echo time
TR – Repetition time
TSE – Turbo spin echo
UTE - Ultra short time of echo
VMAT – Volumetric modulated arc therapy
VOI – Volume of interest

Introduction

Computed tomography (CT) has been the imaging modality of choice for radiotherapy treatment planning because of traceability to electron density from the Hounsfield unit and excellent geometrical accuracy. However the images suffer from poor soft tissue contrast which makes it difficult to delineate structures of interest. Magnetic resonance imaging (MRI) has great soft tissue contrast, which makes it appealing to use in the radiotherapy treatment planning process. Several studies report that magnetic resonance imaging is the imaging modality of choice for delineating the gross target volumes[1-4]. However, using MRI as the only imaging modality in radiotherapy treatment planning is not a straight forward procedure. MRI suffers from inherent geometrical distortion in the images due to the inhomogeneities in the main magnetic field (figure 1) and non-linearity of the spatial encoding gradient fields. Eddy currents arising from the time variant gradient fields are also contributing to the distortion as well as the object or patient being examined[1].

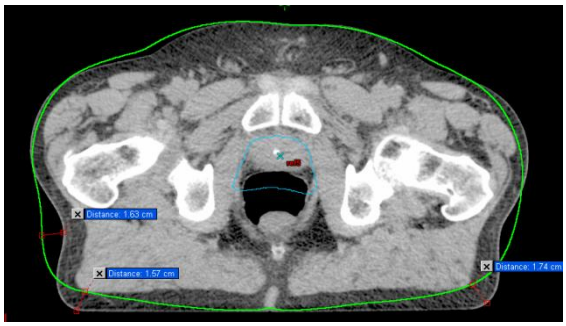

Figure 1. Example of the impact of geometrical distortion on body outlines. The body outline drawn on the MRI image data set (with GDC applied) is shown in green, laid over the CT data. A clear disagreement can be seen.

Besides this, no information of the electron density can be extracted from MRI data. Positioning of the patient using conventional planar image guided techniques is also difficult since digitally reconstructed radiographs cannot be used from an MRI data volume because of the weak signal arising from cortical bone[1,4,5]. However segmenting bone tissue in MRI images can be made more feasible with the help of ultra short time of echo pulses (UTE) which enables the MRI signal from materials with very short T2 relaxation times, such as bone, to be detected[6-9]. A previous master thesis evaluated the feasibility of 3D-3D MRI-Cone beam CT (CBCT) image matching for head treatment with promising results[10]. Prostate cancer patients can also be aligned with the aid of gold implants in the target which are clearly visible on both mega voltage (MV) and kilo voltage (kV) images. They are however not optimized to be used in MRI scanning and are prone to create star artefacts in CT images.

Rationale for the use of MRI in the RTP process

It can be difficult to discriminate adjoining soft tissue structures if they are not separated by fat, air or bone in CT applications. The imaging parameters in MRI scanning are not as limited as with CT scanning, resulting in the ability to vary the soft tissue contrast and enhance differences in proton densities, spin-lattice- (T1) and spin-spin (T2) relaxation times. Adjoining tissue structures with similar attenuation properties can therefore more easily be distinguished if they possess differences in the above mentioned physical properties. Tumours often have similar attenuation properties as the normal soft tissue surrounding it but differ in the T1 and/or T2 relaxation times why an improvement in delineation of target and organs at risk (OAR's) may be achieved[3,11-20]. This results in a more consistent and reliable determination of volumes of interest (VOI's) that is less inter- and intraobserver dependent[19]. MRI also posses the ability to image functional parameters of the tissue which may lead to new strategies in radiotherapy such as biological imaging[21].

Another advantage of MRI is that there is no exposure of non-therapeutic ionizing radiation which is particularly advantageous for paediatric patients and pregnant women.

Results of previous studies

The dosimetric consequences of performing dose planning on MRI only for treatment in the

pelvic region has been evaluated by other investigators with consistent results[4,22-25]. Using a three-field technique for 3D conformal radiotherapy (3DCRT) resulted, for three out of four prostate cancer patients, in a percentage dose difference below 2 % between calculations based on CT and MRI data inside the planning target volume (PTV) when bone and soft tissue was segmented on the MRI images[25]. In the fourth patient, a dose discrepancy was found in a small volume of about 75 mm^3 of maximum 2.7 %. In the same patients when only water equivalent electron density was applied to the volume, the percentage dose differences were mostly greater than 2 % inside the PTV with differences ranging from 0-5 % and sometimes as high as 12 %. In another study where the dosimetric consequences of performing intensity modulated radiotherapy (IMRT) dose planning on MRI and CT of 15 prostate cancer patients were evaluated, a maximum percentage dose difference of 2 % was observed using water density assigned MRI data[4]. Measurements of the IMRT plans resulted in percentage dose differences below 2 % in 13 patients and below 3 % for the other two patients. These studies together with results from studies on the use of MRI dose planning in the skull[22-24] suggests that there is no clinical significant difference when performing dose planning in MRI only compared to that on CT.

Extracting CT-numbers from a CBCT-study could solve the problem of missing Hounsfield units in the MRI-images. One study evaluated the feasibility of cone beam CT based dose planning and concluded that CBCT dose planning was dosimetrically comparable to CT based dose planning[26]. However, CT numbers varied severely due to scatter and reconstruction artefacts. Differences up to 200 Hounsfield units (HU) were observed.

Aim

The purpose of this study is to evaluate the feasibility of an MRI-only radiotherapy clinic for prostate cancer patients by:

- Investigate the performance of the gradient distortion correction algorithm in the MRI scanner
- Evaluate the dosimetric uncertainty resulting from MRI dose planning
- Test the contrast properties of five different marker materials in multimodality applications

The strength of this study is that it incorporates, besides 3DCRT and IMRT, evaluation of a new treatment technique, namely volume modulated radiotherapy (VMAT), which is currently clinically implemented for prostate cancer treatments at Herlev University Hospital.

Theory

This chapter provides a theoretical background to the treatment techniques and MRI image post-processing.

Image distortions in MRI

The image distortion in MRI can be divided into two components; system related inhomogeneities and object induced inhomogeneities[1,27,28]. The system related inhomogeneities are a result of the system design and can be corrected for once the system performance has been established. The object induced inhomogeneities are a result of different magnetic susceptibility throughout the object volume, and therefore object dependent. The subsequent correction has to be calculated for each individual object.

The geometric distortion is affected by different imaging parameters such as the strength, direction and polarity of the gradients. Varying these parameters when imaging an object of known geometry such as a phantom, the system related inhomogeneity of the static field and non-linearity of the gradients can be corrected for. One method is to shift the polarity of the gradient for one of the measurements[29,30]. The error in the static field can be directly quantified assuming the polarity shift inverts the gradient error as well. It is important to understand that this procedure does not incorporate any correction in intensity distortion. It is adequate when contouring the object outlines but is not sufficient when staging target and OAR tissues[27].

One way of correcting the signal intensity distortion is by using the assumption that the integral signal intensity remains constant throughout the image[30]. Mapping the positions in the forward and inverse gradient images can be performed in various ways such as a Runge-Kutta integration[30], dynamic time warping[31], cross-correlation-based model or mutual-information-based model[32]. An exhaustive complete distortion correction for MRI has previously been published[32,33].

In order to account for the distortion related effects, both a phantom study and an in vivo study are required. With the help of the results acquired from the phantom study, the distortion effect due to heterogeneity of the main magnetic field and non-linearity of the gradient fields can be quantified. However, quantifying the distortion is only fruitful if the results are used in a subsequent distortion correction of the images, and if the distortion is mapped in 3D over a sufficiently large volume.

Dosimetric uncertainties in modern radiotherapy

The reason to introduce tolerance levels for the dosimetric uncertainties in radiotherapy is strictly radiobiological. A difference of 7-10 % in delivered absorbed dose to the target results in measurable tumour and normal tissue reactions, according to clinical observations[34,35]. Different tolerance levels have been proposed in the literature in order to ensure adequate tumour control, converging towards a tolerance of 3.0-3.5 %[34,36]. An action level of 5 % has been proposed[36]. The purpose of the action level is if a total uncertainty above this level is detected, comprehensive work should be employed in order to rectify the sources of error. When eradication of the tumour is desirable, an accuracy of 5 % in delivered absorbed dose to the target volume has been recommended[34]. It has also been stated that less than 2 % dose difference in points of relevance to the treatment is an acceptable accuracy of a computer calculated dose distribution if compared to relative measurements[37]. The source of error deduced from absorbed dose calculation algorithms should therefore not be greater than 2 %.

A way of quantifying the total uncertainty is to analyze the uncertainty in the different links in the radiotherapy treatment chain. A summarized result is given in table 1[38].

Table 1. *Estimates of the uncertainty related to the different links in the radiotherapy treatment chain and determination of accuracy goals in dose calculation.*

Source of uncertainty	Uncertainty in % (1 SD)	
	Present	**Future**
Dose determination at the calibration point	1.5	1.0
Additional uncertainty for other points	1.1	0.5
Beam monitor stability	1.0	0.5
Beam flatness	1.5	0.8
Patient data	1.5	1.0
Beam and patient setup	2.5	1.6
Overall excluding dose calculation	3.9	2.4
Dose calculation with heterogeneity correction	1.0/2.0/3.0/4.0/5.0	1.0/2.0/3.0
Overall with heterogeneity correction	4.0/4.4/4.9/5.6/6.3	2.6/3.1/3.8

The acceptance criteria of 3.0 or 3.5 % is not met today even without the uncertainty introduced by the absorbed dose calculation. Setting the tolerance at 5 % allows for an uncertainty in the dose calculation of up to 3 %, which is more reasonable. Hopefully better and more stable linear accelerators and more accurate ionization chambers in the future will help reduce the total uncertainty to the levels presented in table 1.

When introducing MRI dose planning, a new uncertainty is incorporated to the total uncertainty. It also removes the uncertainty inherent from the image registration process but this reduction of the uncertainty is ignored in order to present the worst case scenario. Table 2 presents the total uncertainty when MRI dose planning is used.

Table 2. *Determination of the total uncertainty when MRI dose planning is introduced to the radiotherapy treatment chain. Based on the estimates in table 1.*

Additional uncertainty inherent from MRI dose planning [%]	Uncertainty due to dose calculation with heterogeneity correction	
	1.0/2.0/3.0/4.0/5.0	**1.0/2.0/3.0**
	Present	**Future**
1.0	4.1/4.5/5.0/5.7/6.4	2.8/3.3/4.0
2.0	4.5/4.8/5.3/5.9/6.6	3.3/3.7/4.3
3.0	5.0/5.3/5.8/6.3/7.0	4.0/4.3/4.9
4.0	5.7/5.9/6.3/6.9/7.5	4.8/5.1/5.5
5.0	6.4/6.6/7.0/7.5/8.1	5.6/5.9/6.3

Assuming a 2 % uncertainty in the calculation algorithm when used on CT data, an additional uncertainty of 2.4 % due to the MRI dose planning step fulfils the 5 % dose difference criterion if used today. Using the estimates for the future and 2 % uncertainty in the calculation algorithm allows for a 3.9 % uncertainty in the MRI dose planning step in order to retain the maximum deviation of 5 %. Using a more strict total uncertainty of 3 % eliminates the possibility of MRI dose planning if the uncertainty in the dose calculation algorithm exceeds 1 %. This is however not an unthinkable scenario in the future.

3D conformal radiotherapy, 3DCRT

The introduction of computer controlled multileave collimators (MLC) have enabled treatments where the field edges can quickly be shaped to any target volume, avoiding unnecessary irradiation of OAR's and speeding up treatments due to near elimination of field- and patient specific mould accessories. Computer-aided dose planning using beams eye views (BEV's) allows for shaping the individual beams around the projection of the target volume, hence the term "conformal" in 3DCRT. The 3DCRT treatment technique is still dependent on forward planning, with a trial-and-error approach of finding the best plan.

Intensity modulated radiotherapy, IMRT

In situations where the target volume has a complex shape, such as a concave shape instead of spherical one or OAR's are situated nearby, conformity is especially important. Consider the case with a tumour wrapping itself around the spinal cord. A traditional three dimensional conformal radiotherapy treatment cannot create the concave dose distribution required for such a treatment to be beneficial for the patient. IMRT utilize an inverse dose planning calculation algorithm to find optimized beam intensity maps that incorporates the three dimensional information about the structures in the patient. Various ways has been suggested in the literature on how to acquire the optimized intensity maps, or beamlet matrices, such as a deconvolution method[39-41] where the beamlet matrices are deconvolved from the desired dose matrix. The mathematical operation is simple, but generates negative beamlet weights, which of course is impossible to achieve. Another way of acquiring the beamlet matrices is by an iteration method based on the difference between the prescribed dose and the resulting dose for a given set of beamlet weights. The iteration optimization step requires two conditions:

1. One or more goals
2. An objective function

A goal can be formulated in various ways, such as a dose volume histogram (DVH) goal[42]. A DVH goal can e.g. be a minimum target volume that should receive a given dose or more. The objective function is a measure of how far away the iteration is from a given goal.

The dose calculation equation for an IMRT plan can be written as[43]:

$$d_i = \sum_{j=1}^{M} D_{ij}\, w_j \qquad [14]$$

where d_i is the absorbed dose to the *i*:th voxel, *j* is the beamlet index, D_{ij} is the dose to voxel *i* from the *j*:th beamlet w_j. The inverse dose planning step finds a vector *w* containing all optimized beamlet weights.

The objective function can be formulated in different ways depending on which structure volume the function is applicable to. An example of such a function is the quadratic objective function[43]:

$$f_0(x) = \sum_{i=1}^{N} s_i \left(d_i - d_i^{pres}\right)^2 \qquad [15]$$

where there are N voxels where $f_0(x)$ is applicable, for the *i*:th voxel: s_i is the penalty, d_i is the resultant dose and d_i^{pres} is the prescribed dose. It is then clear that by minimizing the objective function, an optimum solution is found. This statement is only valid if $f_0(x)$ is a convex function with a global minimum value. If not, there is a risk of finding a local minimum which might not represent the best solution.

When an optimized beamlet weight vector is found, it should be realized into deliverable fluence maps via the MLC aperture. This is done via an algorithm that converts the fluence maps into leaf positions as a function of the monitor units. There are two ways the intensity modulated maps can be realized. When the radiation is given in interval steps with the MLC leaves moving in between, this is called the step-and-shoot technique. When the leaves are moving during the beam delivery, this is called dynamic technique.

Volumetric modulated arc therapy, VMAT

VMAT is a treatment technique that evolved from the initial idea of a rotational IMRT treatment technique called Intensity modulated arc therapy (IMAT)[44]. IMAT uses a series of arcs with fixed gantry rotation speed, fixed dose rate and MLC-shapes derived using the optimization procedure for the IMRT treatment technique, in order to provide plans better than those acquired using IMRT. By modulating not only the intensity profiles but also the gantry rotational speed and the dose rate, it is possible to deliver an entire fraction of 2 Gy in a single arc only, yet still remain an equivalent or better dosimetric quality than IMRT[45,46]. This technique is called VMAT and is employed by

Elekta under the same name and by Varian as RapidArc®. Due to the nature of the radiation delivery, it is possible to reduce the treatment times significantly which has the potential to reduce intra-fractional differences and to increase the work flow in a radiotherapy department, alternatively free up time for e.g. image guidance[47]. The main radiobiological concern of this treatment technique is the "dose smearing effect". Using VMAT increases the volume irradiated, thus increasing the concern of detrimental long term effects of the radiation. This must be taken into consideration when deciding what specific treatment technique will benefit the patient the most.

Materials and methods

The three parts of this study is separately described in this chapter.

Evaluation of the gradient distortion correction (GDC) algorithm of an open 1T MRI scanner

The in vivo study does not generate quantifiable results, only relative results in terms of comparison of the distortion effect on image sets acquired with and without the help of GDC.

MRI imaging parameters

The MRI unit used for this study is a Phillips Panorama HFO 1.0T system with an open bore design and a flat tabletop (figure 2).

Figure 2. Phillips Panorama HFO MRI system installed at Herlev university hospital with external laser positioning system.

The open bore design allows for a flat tabletop and fitment of patient immobilization accessories for use in the radiotherapy treatment process. The imaging parameters used in the study of the geometrical distortion can be found in table 3.

Table 3. *Imaging parameters for the geometrical distortion evaluation study.*

Parameter	Value
Pulse sequence	T2W-TSE
ETL	24
TR	1116 ms
TE	110 ms
Slice thickness	3 mm
Slice gap	0 mm
# Slices	5
Imaging direction	Varying (see figure 4-6)
Resolution	1024x1024
FOV	530 mm
Coil type	Body

Phantom study

Phillips supplied the MRI system with a geometrical distortion evaluation phantom, consisting of liquid filled tubes aligned equidistantly from each other in a two dimensional array. The spatial dimensions of the phantom and the tube spacing are illustrated in figure 3. The geometrical distortion can be evaluated in all three dimensions by imaging the phantom in all three planes. This was done by using the accompanying fastening accessories (figure 3-6).

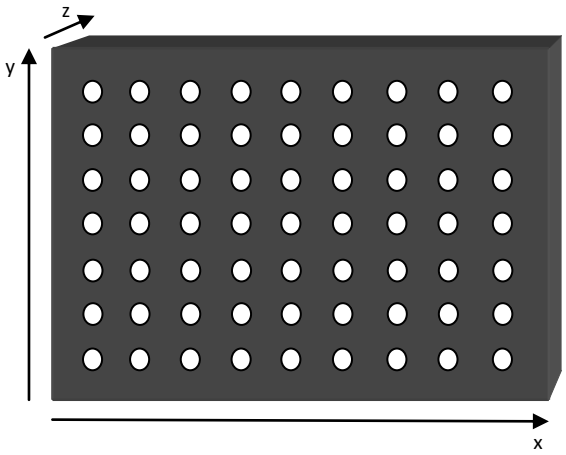

Figure 3. Illustration of the spatial properties of the geometric distortion evaluation phantom. Length (x) = 43 cm, height (y) = 36 cm and depth (z) = 3 cm. The spacing between the liquid filled tubes is 25 mm. The diameter of each tube is 9 mm.

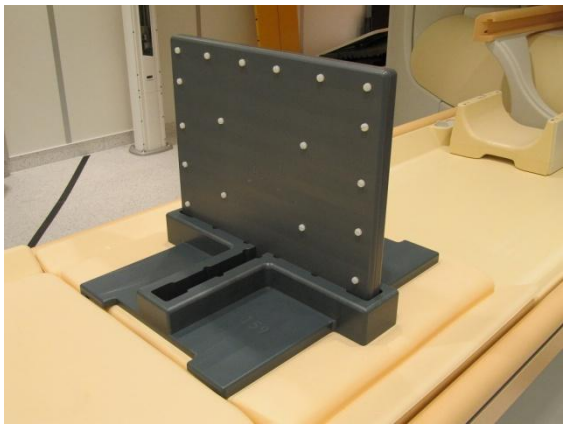

Figure 4. Geometrical distortion evaluation phantom provided by Phillips. Transversal orientation.

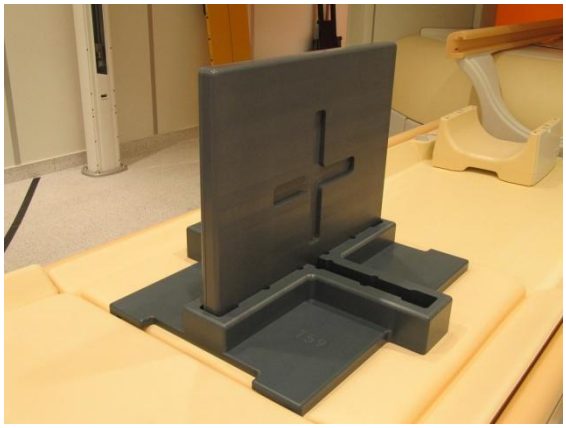

Figure 5. Geometrical distortion evaluation phantom provided by Phillips. Sagittal orientation.

Figure 6. Geometrical distortion evaluation phantom provided by Phillips. Coronal orientation.

In vivo study of healthy volunteers

Three healthy volunteers were chosen for this study. They were imaged using the standard clinical protocol for prostate cancer diagnostics (table 4) with and without the GDC algorithm enabled. The images were then imported into Eclipse® radiotherapy treatment planning (RTP) in order to segment the body contours. The body contours segmented on the image data set acquired with the GDC algorithm disabled was laid on top of the image data set acquired with the GDC algorithm enabled in order to study the difference in body contours.

Table 4. *Imaging parameters used in the clinical routine scanning of prostate cancer patients and used for the three healthy volunteers and for the four volunteer patients in the marker visibility study.*

Parameter	Value	Value
Pulse sequence	TSE	FFE
ETL	24	-
TR	3800	600
TE	110 ms	16
Slice thickness	2 mm	4 mm
Slice gap	0 mm	0 mm
# Slices	Varying*	Varying*
Imaging direction	Transversal	Transversal
Resolution	864x864	960x960
FOV	250 mm (AP), 399 mm (RL), 98 mm (FH)	240 mm (AP) 399 mm (RL) 88 mm (FH
Coil type	XL	XL

*Depending on size, shape and position of the target and patient

Dosimetric investigation of MRI dose planning

Ten patients were randomly chosen for this study and plans were generated using a 4-field box shaped 3DCRT treatment technique, 5-field IMRT treatment technique and singe-arc VMAT treatment technique. Informed consent was acquired from all subjects. The dose discrepancies resulting from assigning unit and bulk densities to the treatment volume rather than using object specific electron densities was evaluated both globally and locally.

The process of segmenting bone on MRI data automatically was not possible with the software provided why this process was performed on the CT data by using the built-in automatic segmentation algorithm for bone tissue for CT-image data in the RTP system. The body outlines were also found automatically using an automated body contour finding algorithm, which was found usable for both CT and MRI image data sets. The structures delineated on CT-images was transferred to the MRI images with the help of the treatment planning system which allows CT-MRI image registration (figure 7).

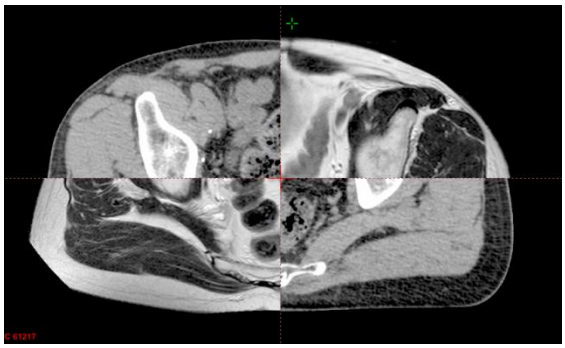

Figure 7. Example of the result of a CT-MRI image registration.

This simulates the process of using automatic segmentation algorithms on the MRI data. This fusing process is the golden standard today for prostate cancer treatment planning where the target and OAR are delineated on the MRI images and transferred to the CT-images[1,4]. The disadvantage of this procedure is that it incorporates an uncertainty in the process because of difficulties aligning the images and of different rectal and bladder filling between the scans[1,4,48].

Dose calculations were first performed on the CT data only using the clinical dose plan available since the patient group studied consisted of patients who already had received treatment. The dose plans were therefore optimized on the CT data with inhomogeneity correction. The treatment parameters including the monitor units and collimator leaf positions was then used on the MRI data where all voxels were assigned as either water density or water and bone density. The HU value calculated for bony structures emanates from the electron density of the sacrum for men at the age of 90, and was found to be 403 HU[49]. Water receives a Hounsfield value of 0, according to the definition of the HU-unit. The resultant dose distributions for the dose calculations was compared to those acquired on the CT data in order to evaluate the consequences of missing inhomogeneity correction and geometric distortion (figure 8).

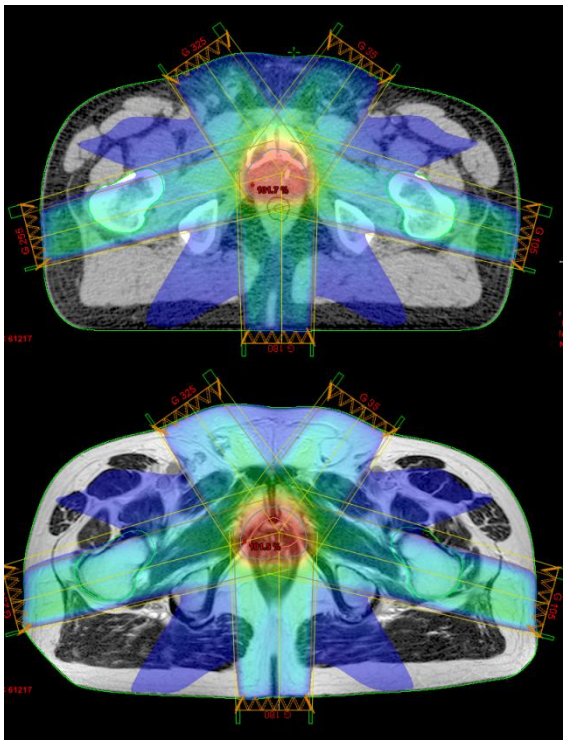

Figure 8. Example of an IMRT plan optimized and calculated on the CT data (top) and then calculated on unit density assigned MRI data (bottom). Absorbed dose distribution is shown in color wash.

The RTP software used was Varian Eclipse® v8.9 and when exporting absorbed dose distributions in the DICOM format, the dose distributions retained the reference system for the modality from which the image data was generated. Since the point of origin in the CT scanner and the MRI scanner are placed at different positions, the resulting dose distributions were not comparable. To solve this problem, the dose distributions calculated on the CT data had to be shifted and rescaled to fit the coordinate system of the dose distributions calculated on the MRI data before any matrix operations were performed. The corresponding translation in the x, y and z direction was given by the RTP system when the image data from both modalities had been registered and matched. Rotation was ignored due to the small angles (< 1°) of the fit[50]. Dose volume histograms (DVH's) were also studied.

Dose distributions calculated on attenuation corrected CT data (abbreviated "CT") and homogenous density assigned CT data (abbreviated "CT_{water}") was compared and gives information of the contribution to the uncertainty in the dose calculation resulting from ignoring tissue heterogeneity. Comparison of the dose distributions calculated on the CT_{water} data and the water assigned density MRI data (abbreviated "MRI_{water}") gives information of the contribution to the uncertainty in the dose calculation resulting from the difference in body contours, which are a result of the geometric distortion and also incorporates inter-fractional differences. Distinguishing these two effects is difficult and requires an MRI-CT multimodality where the patient is transferred from one modality to the other in a way that does not compromise the patient positioning.

The total dose difference for unit density assigned MRI data was quantified by comparing the dose distributions calculated on CT and MRI_{water}. The difference was then compared to that calculated on CT and MRI data with water and cortical bone assigned densities (abbreviated MRI_{bones}).

CT imaging parameters

All prostate cancer patients undergo a pre-treatment CT scan on a Phillips Brilliance® Big Bore® CT-scanner using the imaging parameters described in table 5.

Table 5. *Imaging parameters for patients scheduled for prostate cancer treatment.*

Parameter	Value
Tube voltage	120 kV
Slice thickness	2 mm
Pixel size	0,91x0,91 mm^2
Image size	512x512

Beam characteristics

For all three treatment techniques, 15 MV photon beams were implemented with a dose rate of 400 monitor units per minute. VMAT uses modular dose rate with a maximum of 600 monitor units per minute. Absorbed dose distributions were calculated using Eclipse® RTP version 8.9 with the AAA beam model utilizing depth dose curves and dose profiles from a Varian Clinac® iX implemented in the clinic.

Point dose evaluation

Point dose differences such as the maximum dose and minimum dose within the target and mean dose in target relative to the normalization value has been studied.

Root-mean-square evaluation

The root-mean-square values (rms) was calculated in accordance with equation 12 below for volumes enclosed by isodose levels of 60%, 70%, 80%, 90%, 95% and 100% and serves as a relative global dose difference within the volume studied[25].

$$rms_{(D_{CT}-D_x)} = \sqrt{\frac{\sum_{i=1}^{n}\left(D_{CT\,i}-D_{x_i}\right)^2}{n}} \qquad [12]$$

where D_{CT} is the absorbed dose matrix calculated on the CT data and D_x is the absorbed dose matrix calculated for the data of which comparison is intended. $D_{CT,I}$ is voxel *i* in the absorbed dose matrix calculated on the CT data and $D_{x,i}$ is the corresponding voxel in the absorbed dose matrix in the comparison data, and n is the number of voxels within the isodose level volume studied.

Topographical evaluation

The root-mean-square value does not give any spatial information of local dose differences why topographic maps of the percentage dose difference and absolute dose differences was made which provides an oversight of where the dose discrepancies are located within the body. Visually inspecting the absorbed dose distributions is not a good tool of evaluation since they can appear to be identical. The topographical maps are intended to give an idea of where the dose discrepancies can be found in single planes, both in absolute terms and as a percentage dose difference. An example of two different dose distributions can be seen in figure 1 in Appendix I. The definition of the percentage dose differences is as follows using the same notations as in equation 12:

$$D_{\%} = \frac{D_x - D_{CT}}{D_{CT}} \qquad [16]$$

The colour map used in the representations assigns all differences above 3% as dark red and below 3% as dark blue.

3D gamma evaluation of the calculated dose distributions

The gamma evaluation incorporates both a test of the percentage dose difference and a test of the distance to agreement (DTA). The total uncertainty allowed for the dose calculation in order to satisfy the 5 % total dose uncertainty criterion for radiotherapy is 2.4 % as discussed in previous chapters. The criterion for the gamma evaluation was therefore chosen in accordance to be 2 % and 2 mm. The gamma algorithm test if the difference in voxel value for two equivalent voxels in both dose distributions are within 2 %, and if they are not, it test if a voxel value within 2 % can be found within a volume of a sphere with a radius of 2 mm and its centre positioned in the centre of the voxel. The gamma evaluation is passed if a value of less than 1 is assigned to the resulting gamma map and failed otherwise.

Patient positioning using MRI data

This part of the study is divided into two subparts. First, different marker materials were tested for multimodality compatibility. Four volunteer patients were then implanted with the best suited markers in order to test the selected marker material in vivo.

A study of the contrast properties of different marker implants

Five different marker materials where studied in order to find the marker material best suited for both CT and MRI imaging. Two of each type was implanted into two pieces of smoked ham, cylindrical in shape with a diameter of 8 cm and a length of 19 cm (figure 9), according to figure 10.

Figure 9. *The pieces of ham used to house the markers studied. The pieces were marked with skin markers as well in order to find the correct orientation in the resulting images.*

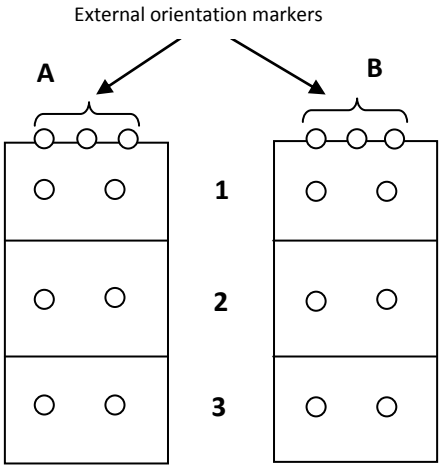

Figure 10. *The relative positions of the different markers. A1 = 24 carat Au, A2 = 18 carat Au/Cu, A3 = 24 carat Au/Fe, B1 = Au/nitinol* 1×3 mm, B2 = Au/nitinol* 1.2×5 mm and B3 = C/Zr.*

The following markers were studied.

- 24 carat gold markers, "standard", size = 1.0x5 mm
- 18 carat gold/copper marker, "red gold", size = 1.0x5 mm
- 24 carat gold/iron markers, size = 1.0x5 mm
- BEAMPOINT BeamMarks® gold/nitinol* markers, size = 1.0x3 mm and 1.2x5 mm
- CIVCO ACCULOC® carbon/zirconium marker, size = 1.0x3 mm

*Nitinol is a metal alloy consisting of approximately 50 % nickel and 50 % titanium

The ham phantoms were then imaged using the parameters listed in table 6 to 8.

Table 6. *Imaging parameters used for the CT scan of the ham.*

Parameter	Value
Tube voltage	120 kV
Slice thickness	2 mm
Pixel size	0.36x0.36 mm^2
Image size	512x512
Imaging direction	Transversal

Table 7. *Imaging parameters used for the T2 weighted MRI scan of the ham.*

Parameter	Value
Sequence type	TSE
ETL	24
TR	2906 ms
TE	110 ms
Slice thickness	2 mm
Slice gap	0 mm
# Slices	95
Imaging direction	Transversal
Pixel size	0.47x0.47 mm^2
Image size	512x512

Table 8. *Imaging parameters used for the T2* weighted MRI scan of the ham.*

Parameter	Value
Sequence type	FFE
TR	600 ms
TE	19 ms
Slice thickness	2 mm
Slice gap	0 mm
# Slices	95
Imaging direction	Transversal
Pixel size	0.42x0.42 mm^2
Image size	560x560

The phantoms were also imaged with the on-board kV, MV and CBCT imaging systems.

Four volunteer patients were implanted with the best suitable marker material and imaged using the scanning parameters presented in table 4. Informed consent were acquired from all subjects.

Feasibility of a marker match in vivo using MRI data only

The hypothesis to be tested is that it should be possible for the software at the linear accelerator to be able to accept an MRI-based treatment plan and that images used for IGRT acquired at the linear accelerator could be used for matching against the MRI images in the treatment plan. The matching results should be within acceptable limits. Modification of the DICOM header of the MRI images was required for the linear accelerator software to accept it, where the modality type was manually changed to CT instead of MRI.

Results and discussion

The results of the study is presented and discussed in this chapter.

Phantom study of the geometrical distortion

Several previous investigators of the geometrical distortion effect in MRI applications recognize the need of a three dimensional phantom in order to fully map the distortions in an environment covering a volume equivalent to that of a pelvis[21,33,48,51,52]. One report provided detailed instructions on a design of a linearity test object[51]. Such a phantom was desirable in this study but was excluded in favour of the two dimensional geometrical distortion evaluation phantom provided by Phillips due to the strict time schedule.

The resulting images acquired with and without the GDC algorithm enabled can be seen in figure 2 in Appendix I (transversal orientation only). Some residual geometrical distortion post-GDC for phantom measurements can be seen in the edges of the phantom but overall the GDC restores the correct spatial coordinates quite satisfactory. The unprocessed image shows severe geometrical distortion over the field of view (FOV) and the GDC algorithm is definitely required before any spatial information of the object is extracted from the images.

In vivo study of the geometrical distortion

A clear disagreement is found for all three volunteers (figure 3 through 8 in Appendix I – Figures and graphs) but no body contour was drawn on volunteer number three due to the severe effect of geometric distortion and to the fact that the FOV did not cover the entire body.

The largest discrepancies are located in the posterior periphery due to the distance from the magnetic isocentre being the farthest at this point. For the VMAT treatment technique, this can be harvested by omitting these angles in the beam arc, and theoretically reduce the dose discrepancies when performing MRI dose planning. For the 3DCRT and the IMRT treatment technique, aligning beams through these areas should be avoided if possible.

Point dose evaluation

There is mainly one OAR when treating the prostate. The rectum is situated at the posterior side of the prostate why the maximum and mean dose in this organ is studied. For the target, the maximum, minimum and mean dose are studied for the three treatment techniques.

Table 9. *Mean percentage deviation in the maximum, minimum and mean dose in the PTV of the target for the 3DCRT treatment technique for all patients compared to CT. Values in brackets are the largest value in that group.*

	MRI_{water}	**MRI_{bones}**
Maximum dose	1.2 ± 0.8 (2.4)	-0.3 ± 0.5 (-1.2)
Minimum dose	-0.6 ± 8.5 (15.8)	-1.9 ± 8.8 (-18.3)
Mean dose	1.6 ± 0.8 (2.8)	0.0 ± 0.5 (0.9)

There is a significant ($p < 0.05$) difference between MRI_{water} and MRI_{bones} for the maximum and mean absorbed dose in the PTV where the latter is clearly the better alternative, being more similar to the original dose distribution. For the rectum, the result is not statistically significant ($p = 0.95$).

Table 10. *Mean percentage deviation in the maximum, minimum and mean dose in the PTV of the target for the IMRT treatment technique for all patients compared to CT. Values in brackets are the largest value in that group.*

	MRI_{water}	**MRI_{bones}**
Maximum dose	-0.2 ± 0.6 (-1.2)	-0.9 ± 0.6 (-1.5)
Minimum dose	-7.5 ± 7.2 (-19.2)	-10.5 ± 8.6 (-24.9)
Mean dose	-0.3 ± 0.5 (1.1)	-1.3 ± 0.4 (-2)

Again, there is a significant difference ($p < 0.05$) between the maximum and mean dose for MRI_{water} and MRI_{bones} for the PTV, and no statistically significant result for the rectum ($p = 1$).

Table 11. *Mean percentage deviation in the maximum, minimum and mean dose in the PTV of the target for the VMAT treatment technique for all patients compared for CT. Values in brackets are the largest value in that group.*

	MRI_{water}	MRI_{bones}
Maximum dose	0.2 ± 0.5 (0.8)	-0.4 ± 0.5 (-1.2)
Minimum dose	-11.4 ± 11.9 (-28)	-12.9 ± 13.8 (-38.6)
Mean dose	0.8 ± 0.7 (2)	-0.1 ± 0.5 (-0.8)

The results indicate, as with the 3DCRT and IMRT treatment techniques, that there is a significant difference ($p < 0.05$) between the maximum and mean absorbed dose in the target PTV but not for the rectum.

Root-mean-square evaluation of the calculated dose distributions

An important consequence of the matrix rescale and shifting procedure previously described is that the rms values calculated include the uncertainty inherent from the MRI-CT image matching process in the RTP. However, since the rms method of evaluation is relative, this is not a problem. It will however contribute to the percentage and absolute dose differences.

The rms values were calculated for each patient, isodose level and treatment technique. The mean for each isodose level and treatment technique was computed and is presented in table 12 through 14 respectively. Figures of the corresponding graphs can be viewed in figure 9 through 11 in Appendix I. It should be emphasized that the rms values are not directly linked to clinical relevance, e.g. a large rms value compared to a low rms value does not necessarily mean that the latter one is better. Figure 10 and 11 illustrates an example of this.

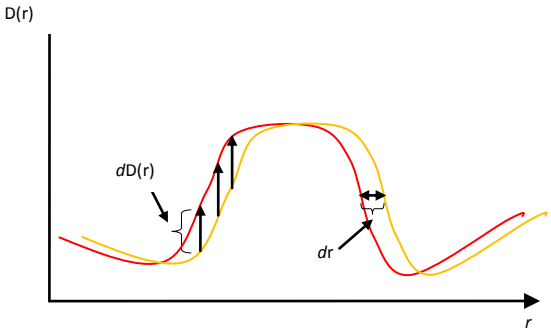

Figure 10. Example of a 2-dimensional dose distribution where a small shift d*r*, also called distance-to-agreement (DTA), results in large deviations d*D*(*r*) which in turn leads to a large contribution in the summation of the square of the differences according to equation 12.

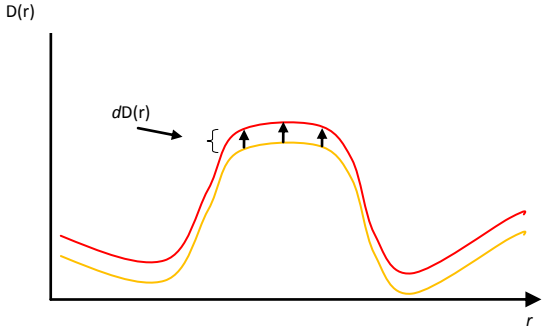

Figure 11. Example of a 2-dimensional dose distribution where the contribution to the rms value due to the difference in absorbed dose is illustrated.

In figure 10 and 11 above, two similar dose profiles are illustrated where the case in figure 10 results in a larger rms value than the case in figure 11. Depending on the size of d*r* and d*D*(*r*), the difference in the example in figure 10 may be clinically insignificant while the difference in the example in figure 11 may be unacceptable why the evaluation of the feasibility of MRI dose planning must include other ways of evaluation as well.

Table 12. *Mean-rms values calculated for the 3DCRT treatment technique for different volumes enclosed by isodose levels (rows) and between plans which are to be compared (columns).*

	CT/CT_{water}	CT_{water}/MRI_{water}	CT/MRI_{water}	CT/MRI_{bones}
60 %	0.9 ± 0.2	2.0 ± 0.8	2.2 ± 0.7	1.9 ± 0.8
70 %	0.9 ± 0.2	1.8 ± 0.9	2.0 ± 0.7	1.7 ± 0.9
80 %	1.0 ± 0.3	1.7 ± 1.1	2.1 ± 0.8	1.6 ± 1.0
90 %	1.0 ± 0.4	1.0 ± 0.5	1.5 ± 0.5	0.9 ± 0.5
95 %	1.0 ± 0.4	0.7 ± 0.3	1.4 ± 0.4	0.6 ± 0.2
100 %	1.0 ± 0.5	0.4 ± 0.2	1.3 ± 0.5	0.4 ± 0.1

There is a significant ($p < 0.05$) decrease in the rms values for smaller volumes studied and there is also a significant difference ($p < 0.05$) between the dose distributions calculated on MRI_{water} and MRI_{bones} where the last mentioned is better, which was expected due to it being a better approximation to the original CT data. However, when studying the rms values for the IMRT treatment technique, the relation is opposite, with MRI_{water} being the better alternative.

Table 13. *Mean-rms values calculated for the IMRT treatment technique for different volumes enclosed by isodose levels (rows) and between plans which are to be compared (columns).*

	CT/CT$_{water}$	**CT$_{water}$/MRI$_{water}$**	**CT/MRI$_{water}$**	**CT/MRI$_{bones}$**
60 %	0.5 ± 0.2	1.8 ± 0.8	1.6 ± 0.9	2.5 ± 1.3
70 %	0.5 ± 0.2	1.5 ± 0.8	1.5 ± 0.8	2.3 ± 1.2
80 %	0.5 ± 0.2	1.3 ± 0.7	1.3 ± 0.7	1.9 ± 0.9
90 %	0.6 ± 0.2	1.0 ± 0.4	0.9 ± 0.4	1.5 ± 0.6
95 %	0.6 ± 0.2	0.8 ± 0.3	0.8 ± 0.3	1.2 ± 0.4
100 %	0.6 ± 0.2	0.6 ± 0.1	0.6 ± 0.2	1.0 ± 0.3

Table 14. *Mean-rms values calculated for the VMAT treatment technique for different volumes enclosed by isodose levels (rows) and between plans which are to be compared (columns).*

	CT/CT$_{water}$	**CT$_{water}$/MRI$_{water}$**	**CT/MRI$_{water}$**	**CT/MRI$_{bones}$**
60 %	0.7 ± 0.4	2.4 ± 1.4	2.5 ± 1.4	2.5 ± 1.6
70 %	0.7 ± 0.3	2.3 ± 1.3	2.3 ± 1.3	2.3 ± 1.5
80 %	0.7 ± 0.3	2.0 ± 1.1	2.1 ± 1.1	2.0 ± 1.3
90 %	0.7 ± 0.2	1.4 ± 0.8	1.6 ± 0.8	1.5 ± 0.9
95 %	0.6 ± 0.2	1.1 ± 0.6	1.3 ± 0.6	1.1 ± 0.6
100 %	0.6 ± 0.2	0.8 ± 0.4	1.1 ± 0.5	0.9 ± 0.4

The rms values calculated for the VMAT treatment technique are not as conclusive as the results for the 3DCRT and IMRT treatment techniques, where no significant ($p = 0.07$) difference between the rms values calculated for MRI_{water} and MRI_{bones}. However, when studying the calculated rms values for the individual patients, there are two outliers. Patient #8 is the most extreme case as can be viewed in figure 12 in Appendix I. It appears that the approximation of assigning the segmented bone structure a bulk density of 403 HU is worse than assigning unit density to the patient volumes for these two patients. The reason is probably that these patients possess bony tissues in the pelvis region with lower attenuation than expected. This gives rise to, as previously discussed, in an apparent under dosing in the target.

These outliers generate a larger uncertainty to the mean rms-values given in table 14 above, reducing the significance. When studying the rms values for the individual patients (figures 12 through 14 in Appendix I), the difference between MRI_{water} and MRI_{bones} becomes clearer.

Evaluation of the rms values for dose distributions calculated on MRI_{water} and CT_{water} (figure 15 in Appendix I) leads to the conclusion that the largest contribution to the dose discrepancies, when studying larger volumes than the volume enclosed by the 90 % isodose level, comes from the difference in body outlines due to inter-fractional differences and geometric distortion. For smaller volumes the contributions from missing inhomogeneity correction and geometric distortion are of about the same size. Moreover, the contribution from missing inhomogeneity correction is invariant of the volume size in contrast to the contribution from geometric distortion which shows dependence of the volume size.

DVH's

A study of the DVH's for the ten patients reveals a systematic under dosage in the target for the MRI_{bones} plans. An example can be viewed in figure 16 in Appendix I. It is believed that this is a consequence of assigning a bulk density to the segmented bone areas. The IMRT plans differ from the other two treatment techniques in that the fields are aligned to avoid bony areas in the pelvis. The Hounsfield unit calculated for the bony structures may be an over estimate of the actual mean of the bones through which the beams are aligned in the IMRT plans. This will result in a higher attenuation in these areas than in the original CT plan, resulting in an apparent under dosing

in the target (If the IMRT plan would have been optimized on the MRI data, this would actually produce an over dosing in the target due to the over estimation of bone attenuation and the corresponding increase in the number of monitor units). For the 3DCRT plans, the fields are aligned without consideration of bony tissues, resulting in MRI_{bones} being a better approximation to the original CT plan.

Topographical maps of the absolute and percentage dose differences

Patient #3 and #4 are used in this presentation as they are representative of a bad and a good agreement with the original dose distribution.

3D conformal radiotherapy

Large dose discrepancies in the simple 4 field 3DCRT treatment technique appear mostly when the bulk of the cubic shaped dose distribution created in the volume containing the intersected beams is shifted in space due to different body contours in the dose matrices. The dose deviations can be seen at the edges of the fields and in low dose areas (figure 17a and 18a in Appendix I). When a good spatial agreement between the bulk of the dose distributions exist, the dose deviations are mostly prominent in low dose areas (figure 17c and 18b in Appendix I).

As previously shown, the rms values for plans laid on MRI_{bones} are significantly smaller than those laid on MRI_{water} for the 3DCRT treatment technique. This can be seen when comparing the percentage dose distributions in figure 17a and 17b with those in figure 17c and 17d. The difference between MRI_{water} and MRI_{bones} is clear and no dose difference of more than 2 % can be seen within the target in patient #4.

Intensity modulated radiotherapy

The IMRT treatment technique is more complex than the 3DCRT technique studied in this work, utilizing 5 fields in total and optimized field segments (figure 19a in Appendix I). Dose differences can again be seen in and around the field edges for patient #3, given in figure 20a and 20b in Appendix I. For patient #4, low dose areas show greater percentage dose difference than in the area in the target as can be seen in figure 20c and 20d in Appendix I. As previously stated, MRI_{bones} is a worse approximation to CT than MRI_{water} for the IMRT treatment technique for all patients studied, which can be seen in the topographic maps as well.

Volumetric modulated arc therapy

VMAT differs from 3DCRT and IMRT treatment techniques as it does not utilize a set of individual beams (figure 19b in Appendix I). The effect of large percentage dose differences in the field edges is therefore not present in the same way as in the previous examples. Instead, even larger percentage dose differences are present in the low dose areas outside the target area. For patient #3, calculating dose distributions on MRI_{bones} gives no apparent advantage to that calculated on MRI_{water} (figure 21a and figure 21b in Appendix I), which is confirmed when studying the rms values for these two plans. Patient #4 shows a better agreement with the original dose distribution for both MRI_{bones} and MRI_{water} (figure 21c and figure 21d in Appendix I). Moreover, there is a clear visible improvement for MRI_{bones} over MRI_{water}.

3D gamma evaluation

Two example slices of the gamma evaluation resultant matrices are given in figure 22 in Appendix I. The treatment technique used was VMAT and patient #3 and #4 are compared. Patient #3 fail the gamma test in several clinically significant areas but also in clinically insignificant areas (low dose areas outside target and OAR). In low dose areas, the gradients of the absorbed dose distribution are low and the gamma test is failed if there is a local percentage dose difference larger than 2 %. The DTA criteria is in principle only usable in high dose gradients. Patient #4 shows an acceptable agreement but fails the gamma test in the build up regions. This is however not clinically significant.

Contrast properties of different marker implants

The ideal marker material would give rise to both high photon attenuation in X-ray applications and high signal strength in MRI applications, as it then would be easy to differentiate the markers from tissue in both CT and MRI applications. This is not the case with the above tested marker materials. They are all made of different kind of metals possessing relatively high attenuation properties which makes them ideal for CT. They are however only indirectly visible in MRI due to the susceptibility artefacts they give rise to. The best marker would therefore give rise to a susceptibility artefact not to great so that the entire image quality is degraded or to small so that they are invisible. A too large susceptibility artefact also increases the geometric uncertainty of the marker position.

A summarize of the visibility of the different marker implants is given in table 15 below for the CT and MRI scan.

Table 15. *Visibility of the different markers for the imaging modalities, according to a three level classing system where + = good, 0 = acceptable, - = not visible or unacceptable visibility.*

Marker	CT	T2w MRI	T2*w MRI
24 carat Au	0	-	-
18 carat Au/Cu	0	-	-
24 carat Au/Fe	0	0	0
Au/nitinol 1.0x3 mm	+	0	0
Au/nitinol 1.2x5 mm	+	0	0
C/Zr	+	-	-

The results show that the most suited marker material for use in multimodality imaging is the Au/nitinol solution with the 24 carat Au/Fe marker being an alternative. The corresponding images showing the results of the scans can be found in figures 23 through 29 in Appendix I.

In vivo study on the feasibility of a marker match

An MRI based dose plan for one of the volunteer patients was successfully loaded into the linear accelerator image guidance software. The markers had previously been segmented in the RTP and a match between the MRI images and the images acquired with the on-board planar kV X-ray system was done. However, as expected, a systematic offset of the MRI images and the X-ray images were seen. This is due to the definition of the isocentre which is different for MRI and other imaging modalities. This problem is currently being investigated.

Conclusions

MRI dose planning of prostate cancer is indeed feasible if a total tolerance level of 5 % is chosen and if certain precautions are made such as implementing a rigorous quality assurance program and assigning appropriate CT-numbers to bony areas. The largest contribution the dosimetric uncertainty in the entire patient volume resulting from MRI dose planning can be attributed to the geometric distortion in the images. Inside the target PTV, the dosimetric uncertainty due to geometrical distortion is of the same size as the contribution from missing inhomogeneity correction.

A commercially available marker material suitable for both CT and MRI imaging has been found. Patient set-up is feasible when using this marker material for CBCT and kV X-ray on-board imager systems.

Acknowledgements

I would like to thank my supervisors Brian and David for their dedication and support of me and this project.

A special thanks goes out to Richard, without whom I would still be lost in the programming jungle.

A big thanks to Herlev's MR-physicist Rasmus, for helping me out with the MRI-scanner late after working hours.

Thanks to the following foundations for enabling me to present the results of this study at the ESTRO 29 conference in Barcelona, 12-19 September 2010 (see Appendix II for accepted abstract) and to continue my work with MRI only dose planning during the summer of 2010:

"Regementsläkaren Dr. Hartelii stipendiestiftelse"

"John och Augusta Perssons stiftelse"

"Skåneföreningen 1900-års mäns stipendiefond"

References

[1]Khoo V. S., Dearnley D. P., Finnigan D. J., Padhani A., Tanner S. F., Leach M. O., ”*Magnetic resonance imaging (MRI): considerations and applications in radiotherapy treatment planning*”, Radiother Oncol **42**:1-15, 1997

[2]Roach M., Faillace-Akazawa P., Malfatti C., Holland J., Hricak H., “*Prostate volumes defined by magnetic resonance imaging and computerized tomographic scans for three-dimensional conformal radiotherapy*”, Int J Radiat Oncol Biol Phys **35**:1011-1018, 1996

[3]Rasch C., Barillot I., Remeijer P., Touw A., van Herk M., Lebesque J. V., ”*Definition of the prostate in CT and MRI: a multi-observer study*”, Int J Radiat Oncol Biol Phys **43**:57-66, 1999

[4]Chen L., Price Jr R. A., Nguyen T-B., Wang L., Li J. S., Qin L., Ding M., Palacio E., Ma C-M., Pollack A., “*Dosimetric evaluation of MRI-based treatment planning for prostate cancer*”, Phys Med Biol **49**:5157-5170, 2004

[5]Parker C. C., Damyanovich A., Haycocks T., Haider M., Bayley A., Catton C. N., “*Magnetic resonance imaging in the radiation treatment planning of localized prostate cancer using intra-prostatic fiducial markers for computed tomography co-registration*”, Radiother Oncol **66**:217-224, 2003

[6]Reichert L.H.I., Robson D. M., Gatehouse D. P., He T., Chappell E. K., Holmes J., Girgis S., Bydder M. G., “*Magnetic resonance imaging of cortical bone with ultrashort TE pulse sequences*”, Magn Reson Imaging **23**:611-618, 2005

[7]Karlsson M., Karlsson G. M., Nyholm T., Amies C., Zackrisson B., ”*Dedicated magnetic resonance imaging in the radiotherapy clinic*”, Int J Radiat Oncol Biol Phys **74**:644-651, 2009

[8]Robson D. M., Bydder M. G., “*Clinical ultrashort echo time imaging of bone and other connective tissues*”, NMR Biomed **19**:765-780, 2006

[9]Thörnqvist S., “*Initial steps toward MRI-based treatment planning for external radiotherapy*”, M. Sc. dissertation, Department of medical radiation physics, Lund university hospital, 2009

[10]Buhl S., Duun-Christensen A. K., “*Evaluation of 3D/3D MRI-CBCT automatching on brain tumors for online patient setup verification in radiotherapy*”, M. Sc. dissertation, Department of electrical engineering, Technical university of Denmark, 2009

[11]Barentsz J. O., Engelbrecht M. R. W., Wities J. A. M., de la Rosette J. J. M. C. H., van der Graaf M., ”*MR imaging of the male pelvis*”, Eur Radiol **9**:1722-1736, 1999

[12]Heenan S. D., “*Magnetic resonance imaging in prostate cancer*”, Prostate cancer prostatic pis **7**:282-289, 2004

[13]Khoo V. S., Padhani A. R., Tanner S. F., Finnigan D. J., Leach M. O., Dearnley D. P., ”*Comparison of MRI with CT for the radiotherapy planning of prostate cancer: a feasibility study*”, Br J Radiol **72**:590-597, 1999

[14]Wachter S., Wachter-Gerstner N., Thomas B., Goldner G., Kovacs G., Fransson A., Potter R., “*Interobserver comparison of CT and MRI-based prostate apex definition – clinical relevance for conformal radiotherapy treatment planning*”, Strahlenther Onkol **178**:263-268, 2002

[15]Roach M., Faillace-Akazawa P., Malfatti C., Holland J., Hricak H., "*Prostate volumes defined by magnetic resonance imaging and computerized tomographic scans for three-dimensional conformal radiotherapy*", Int J Radiat Oncol Biol Phys **35**:1011-1018, 1996

[16]Kagawa K., Lee W. R., Schulteiss T. E., Hunt M. A., Shaer A. H., Hanks G. E., "Initial clinical assessment of CT-MRI image fusion software in localization of the prostate for 3D conformal radiation therapy", In J Radiat Oncol Biol Phys **38**:319-325, 1997

[17]Sannazzari G. L., Ragona R., Ruo Redda M. G., Giglioli F. R., Isolate G., Guarneri A., "*CT-MRI image fusion for delineation of volumes in three-dimensional conformal radiation therapy in the treatment of localized prostate cancer*", Br J Radiol **75:**603-607, 2002

[18]Stenbakkers R. J. H. M., Deurloo K. E. I., Nowak P. J. C. M., Lebesque J. V., van Herk M., Rasch C. R. N., "*Reduction of dose delivered to the rectum and bulb of the penis using MRI delineation for radiotherapy of the prostate*", Int J Radiat Oncol Biol Phys **57**:1269-1279, 2003

[19]Debois M., Oyen R., Maes F., Verswijvel G., Gatti G., Bosmans H., Feron M., Bellon E., Kutcher G., van Poppel H., Vanuytsel L., "*The contribution of magnetic resonance imaging to the three-dimensional treatment planning of localized prostate cancer*", **45**:857-865, 1999

[20]Krempien R. C., Schubert K., Zierhut P., Steckner M. C., Treiber M., Harms W., Mende U., Latz D., Wannenmacher M., Wenz F., "*Open low-field magnetic resonance imaging in radiation therapy treatment planning*", Int J Radiat Oncol Biol Phys **53**:1350-1360, 2002

[21]Khoo V. S., Joon D. L., "*New developments in MRI for target volume delineation in radiotherapy*", Br J Radiol **79**:2-15, 2006

[22]Ramsey C. R., Oliver A. L., "*Magnetic resonance imaging based digitally reconstructed radiographs, virtual simulation and three-dimensional treatment planning for brain neoplasms*", Med Phys **25**:1928-1934, 1998

[23]Schad L. R., Blüml S., Hawighorst H., Wenz F., Lorenz W. J., "*Radiosurgical treatment planning of brain metastases based on a fast, three-dimensional MR imaging technique*", Magn Reson Imaging **12**:811-819, 1994

[24]Kristensen B. H., Laursen F. J., Lögager V., Geertsen P. F., Krarup-Hansen A., "*Dosimetric and geometric evaluation of an open low-field magnetic resonance simulator for radiotherapy treatment planning of brain tumours*", Radiother Oncol **87**:100-109, 2008

[25]Lee K. Y., Bollet M., Charles-Edwards G., Flower M. A., Leach M. O., McNair H., Moore E., Rowbottom C., Webb S., "*Radiotherapy treatment planning of prostate cancer using magnetic resonance imaging alone*", Radiother Oncol **66**:203-216, 2003

[26]Yoo S., Fang-Fang Y., "*Dosimetric feasibility of cone-beam CT-based treatment planning compared to CT-based treatment planning*", Int J Radiat Oncol Biol Phys **66**:1553-1561, 2006

[27]Bakker C. J. G., Moerland M. A., Bhagwandien R., Beersma R., "*Analysis of machine-dependent and object-induced geometric distortion in 2DFT MR imaging*", Magn Reson Imaging **10**:597-608, 1992

[28]Sumanawera T. S., Glover D. H., Binford T. O, Adler J. R., "*MR susceptibility misregistration correcton*", IEEE Trans. Med. Imaging **12**:251-259, 1993

[29]Chang H., Fitzpatrick J. M., "*Geometrical image transformation to compensate for MRI distortions*", Proc SPIE Med Imaging IV: Image Process **1233**:116-127, 1990

[30]Chang H., Fitzpatrick J. M., "*A technique for accurate magnetic resonance imaging in the presence of field inhomogeneities*", IEEE Trans Med Imaging **11**: 319-329, 1992

[31]Kannengiesser S. A. R., Wang Y., Mark H. E., "*Geometric distortion correction in gradient-echo imaging by use of dynamic time warping*", Magn Reson Med **42**:585-590, 1999

[32]Reinsberg S. A., Doran S. J., Charles-Edwards E. M., Leach M. O., "*A complete distortion correction for MR images: II. Rectification of static-field inhomogeneities by similarity-based profile mapping*", Phys Med Biol **50**:2651-2661, 2005

[33]Doran S.J., Charles-Edwards E.M., Reinsberg S. A., Leach M. O., "*A complete distortion correction for MR images: I. Gradient warp correction*", Phys Med Biol **50**:1343-1361, 2005

[34]International commission on radiation units and measurements (ICRU), "*Determination of absorbed dose in a patient irradiated by beams of X or gamma rays in radiotherapy procedures*", ICRU report 24, 1976

[35]Mijnheer B. J., Batterman J. J., Wambersie A., "*What degree of accuracy is required and can be achieved in photon and neutron therapy*?", Radiother Oncol **8**:237-252, 1987

[36]Brahme A., Chavandra J., Lundberg T., McCullough E. C., Nüsslin F., Rawlinson J. A., Svensson G., Svensson H., "*Accuracy requirements and quality assurance of external beam radiotherapy with photons and electrons*", Acta Oncol **27**:7-76 suppl. 1, 1988

[37]International commission on radiation units and measurements (ICRU), "*Use of computers in external beam radiotherapy procedures with high-energy photons and electrons"*, ICRU report 42, 1987

[38]Wieslander E., "*Verification of dose calculation algorithms in treatment planning systems for external radiation therapy*", Dissertation for the degree of Doctor of Philosophy, department of clinical sciences, Lund, ISBN 91-628-6675-3, 2006

[39]Brahme A., Roos J-E., Lax I., "*Solution of an integral equation encountered in rotation therapy*", Phys Med Biol **27**:1221-1229, 1982

[40]Brahme A., "*Optimization of stationary and moving beam radiation therapy techniques"*, Radiother Oncol **12**:129-140, 1988

[41]Holmes T., Mackie T., Simpkin D., Reckwerdt P., "*A unified approach to the optimization of brachytherapy and external beam dosimetry"*, Int J Radiat Oncol Biol Phys **20**:859-873, 1991

[42]Bortfeld T., Levegrun S., Stein J., Zhang G., Rhein B., Schlegel W., "*Intensity modulation with the "step and shoot" technique using a commercial MLC*", Int J Radiat Oncol Biol Phys **39**:148, 1997

[43]Metcalfe P., Kron T., Hoban P., "*The physics of radiotherapy x-rays and electrons*", ISBN 978-1-930524-36-1, Medical physics publishing, 2007

[44]Yu C. X., Jaffray D. A., Wong J. W., Martinez A., "*Intensity modulated arc therapy: a new method for delivering conformal treatments"*, Radiother Oncol **37**:16 suppl. 1, 1995

[45]Otto K., "*Volumetric modulated arc therapy: IMRT in a single gantry arc*", Med Phys **35**:310-317, 2007

[46]Earl M. A., Shepard D. M., Naqui S., Li X. A., Yu C. X., "*Inverse planning for intensity-modulated arc therapy using direct aperture optimization*", Phys Med Biol **48**:1075-1089, 2003

[47]Bzdusek K., Friberger H., Eriksson K., Hårdemark B., Robinson D., Kaus M., "*Development and evaluation of an efficient approach to volumetric arc therapy planning*", Med Phys **36**:2328-2339, 2009

[48]Fransson A., Andreo P., Pötter R., "*Aspects of MRI image distortions in radiotherapy treatment planning*", Strahlenther Onkol **177**:59-73, 2001

[49]International commission on radiation units and measurements (ICRU), "*Photon, electron, proton and neutron interaction data for body tissues*", ICRU report 46, 1992

[50]Cranmer-Sargison G., "*A treatment planning investigation into the dosimetric effects of systematic prostate patient rotational set-up errors*", Med Dosim **33**:199-205, 2008

[51]Tanner S. F., Finnigan D. J., Khoo V. S., Mayles P., Dearnaley D. P., Leach M. O., "*Radiotherapy planning of the pelvis using distortion corrected MR images: the removal of system distortions*", Phys Med Biol **45**:2117-2132, 2000

[52]Takashi M., Yasushi N., Kaoru O., Masaki K., Yoshiharu N., Norio A., Masahiro H., "*Reproducibility of geometric distortions in magnetic resonance imaging based on phantom studies*", Radiother Oncol **57**:237-242, 2000

Appendix I - Figures and graphs

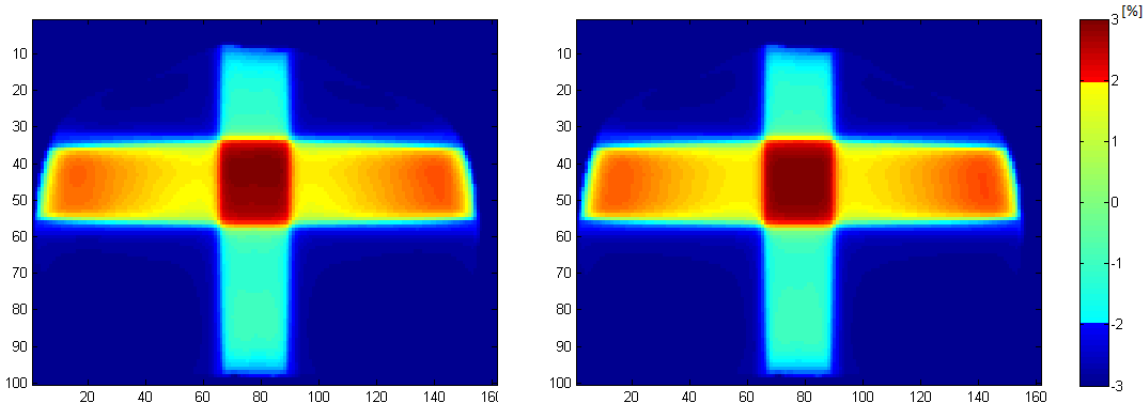

Figure 1. Example of absorbed dose distributions for patient #1 for a 4-field 3DCRT treatment plan calculated for CT and MRI_{water}, respectively. They appear identical why topographical maps are needed to illuminate the deviations.

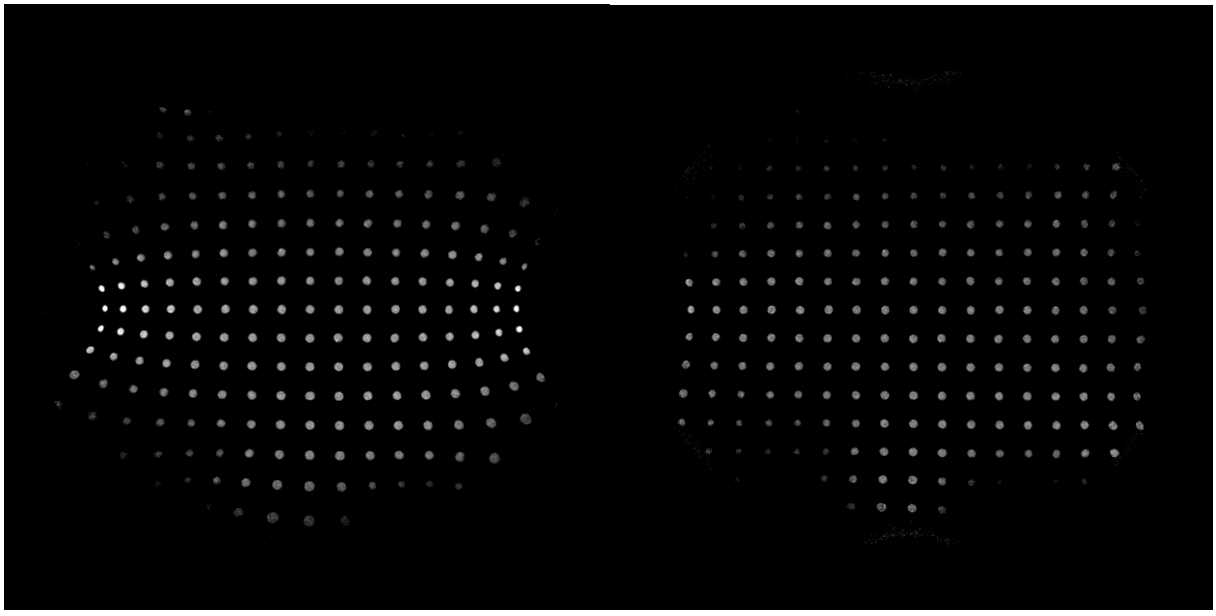

Figure 2. The 2D grid phantom used for gradient distortion evaluation images using a T2W-TSE pulse sequence without GDC enabled (left) and with the GDC enabled (right). The spatial accuracy is increased using the GDC image post-processing technique but some residual distortion can be seen in the edges of the phantom.

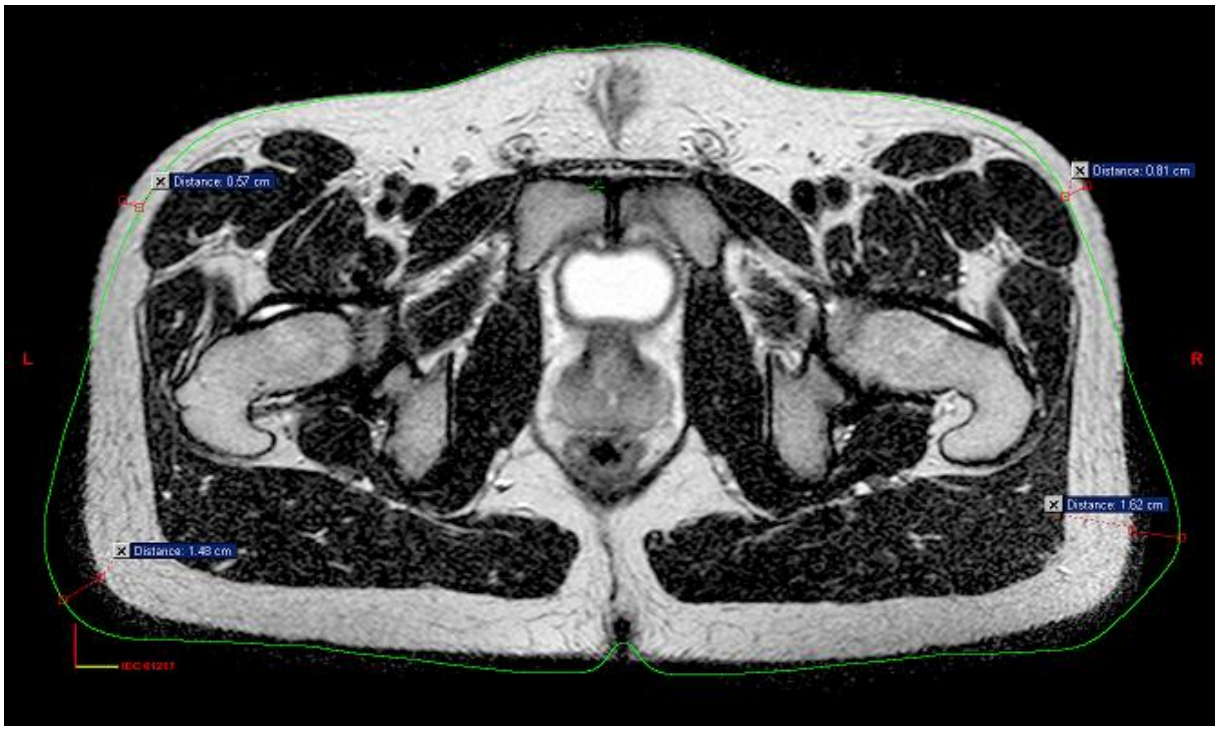

Figure 3. Volunteer #1 showing a disagreement between the body contours when disabling the GDC-algorithm. The green line shows the body outlines for the MRI data volume without the GDC-algorithm enabled. The effect is more severe in points far away from the magnetic isocenter than points close to it, which can be seen in the posterior periphery of the pelvis area. This image was acquired using the TSE pulse sequence.

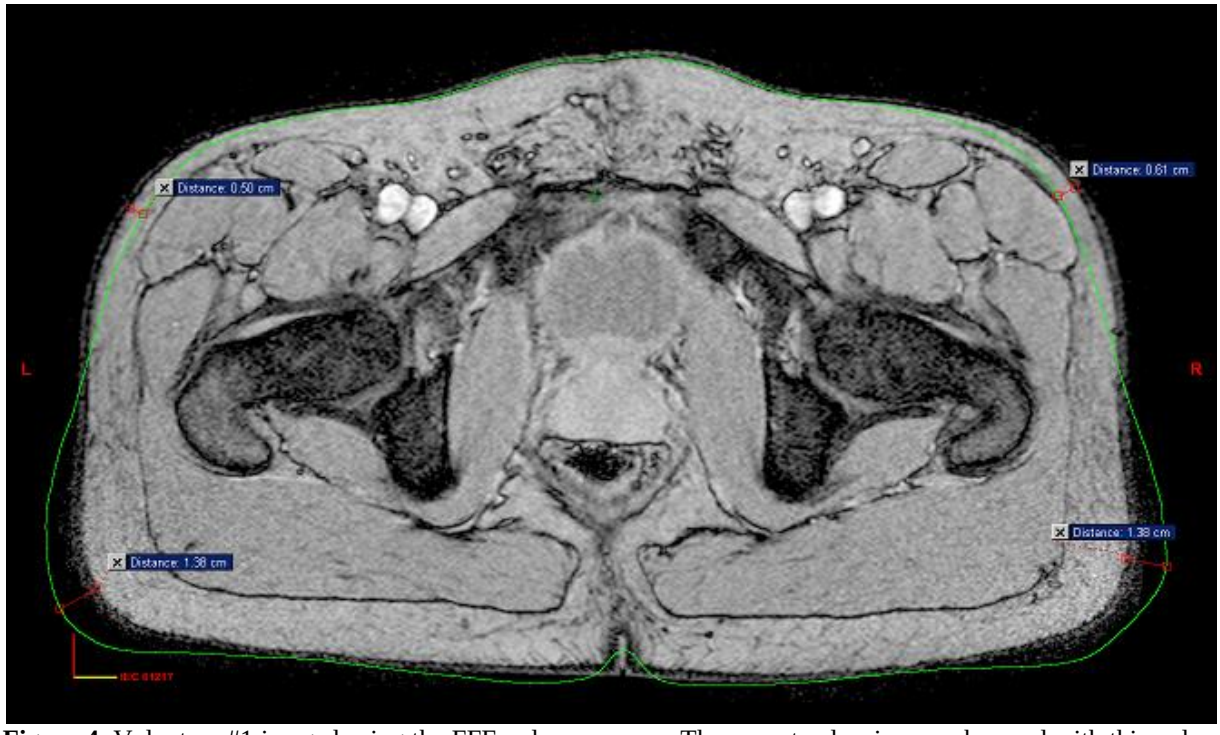

Figure 4. Volunteer #1 imaged using the FFE pulse sequence. The same tendencies are observed with this pulse sequence as with the TSE.

Figure 5. Volunteer #2 imaged with the TSE pulse sequence, head first. The FOV did not fully encapsulate the pelvis which is observed in the far right area.

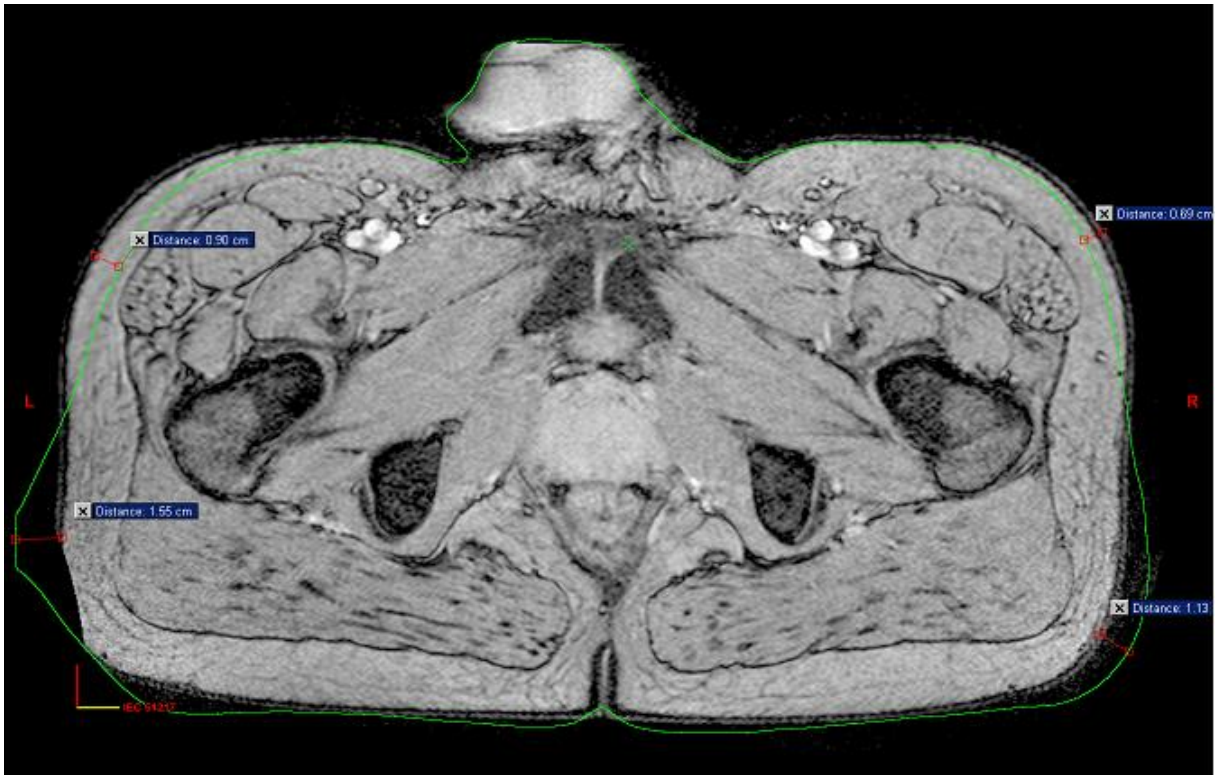

Figure 6. Volunteer #2 imaged with the FFE pulse sequence. The same tendencies are observed with this pulse sequence as with the TSE.

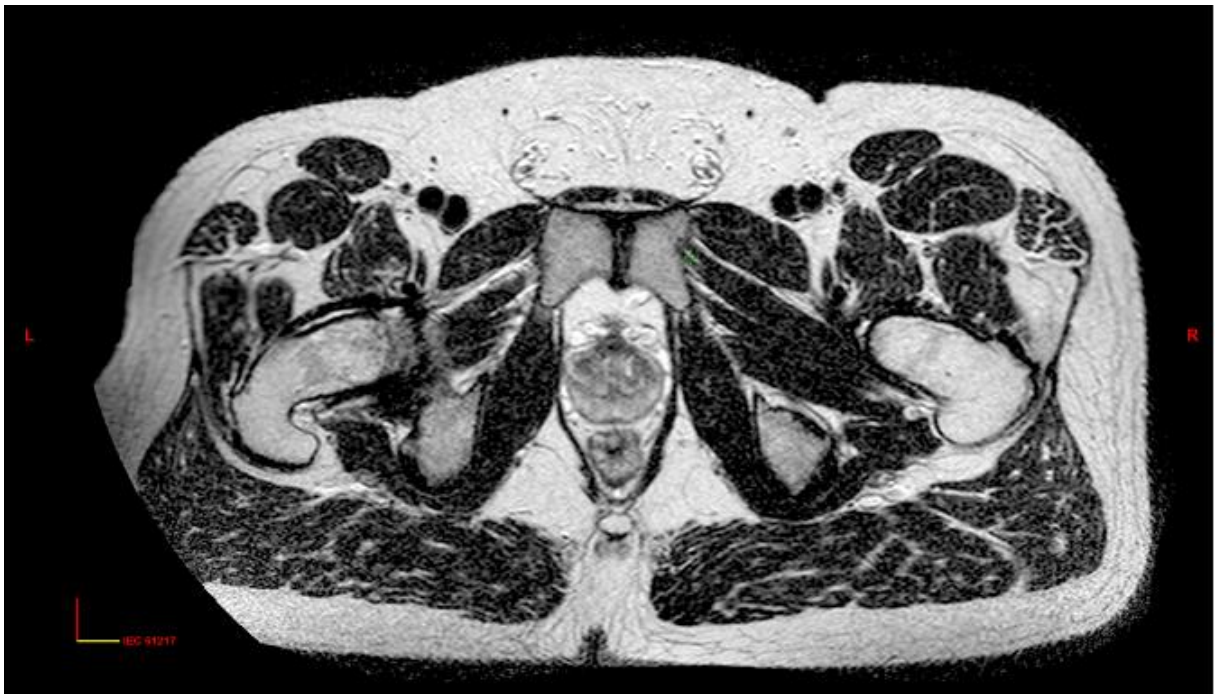

Figure 7. Volunteer #3 imaged with the TSE pulse sequence and the FOV deliberately set to small for encapsulation of the pelvic area. The GDC algorithm fails in compensating for the geometric distortion effect in the right posterior are, which shows as a local "stretching" of the pelvis.

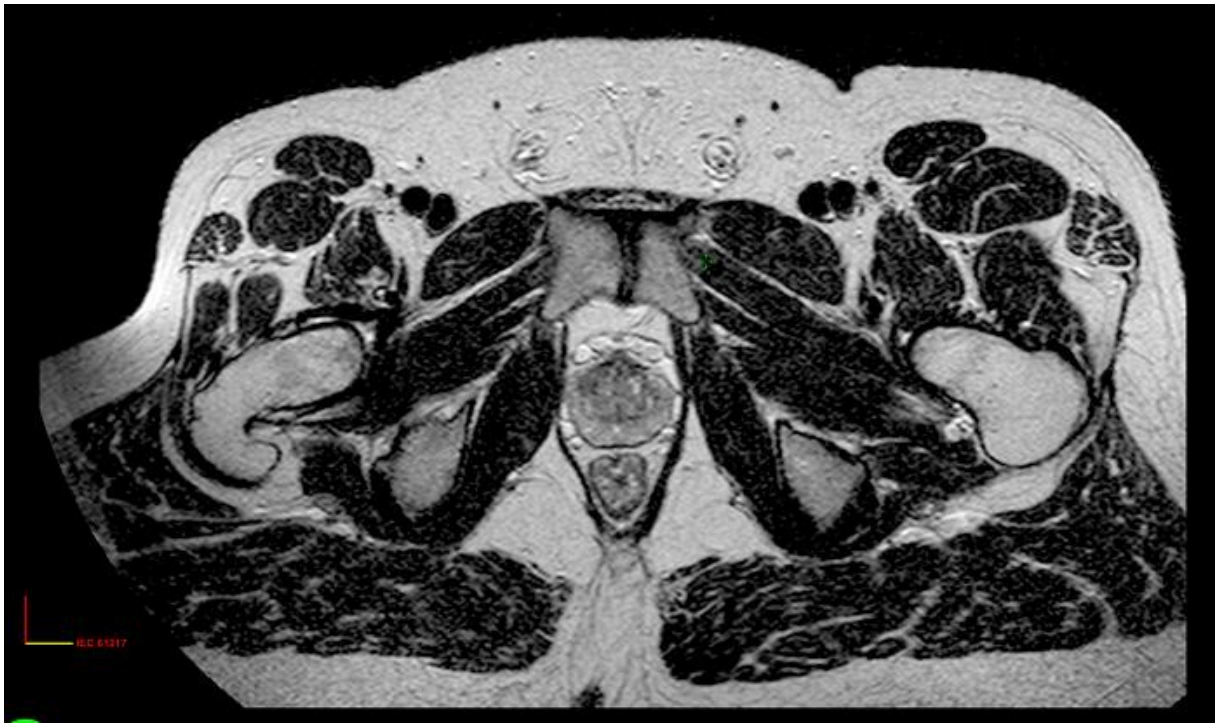

Figure 8. Volunteer #3 imaged with the TSE pulse sequence with the GDC disabled. The effect of geometric distortion is severe in the periphery, especially in the far right area.

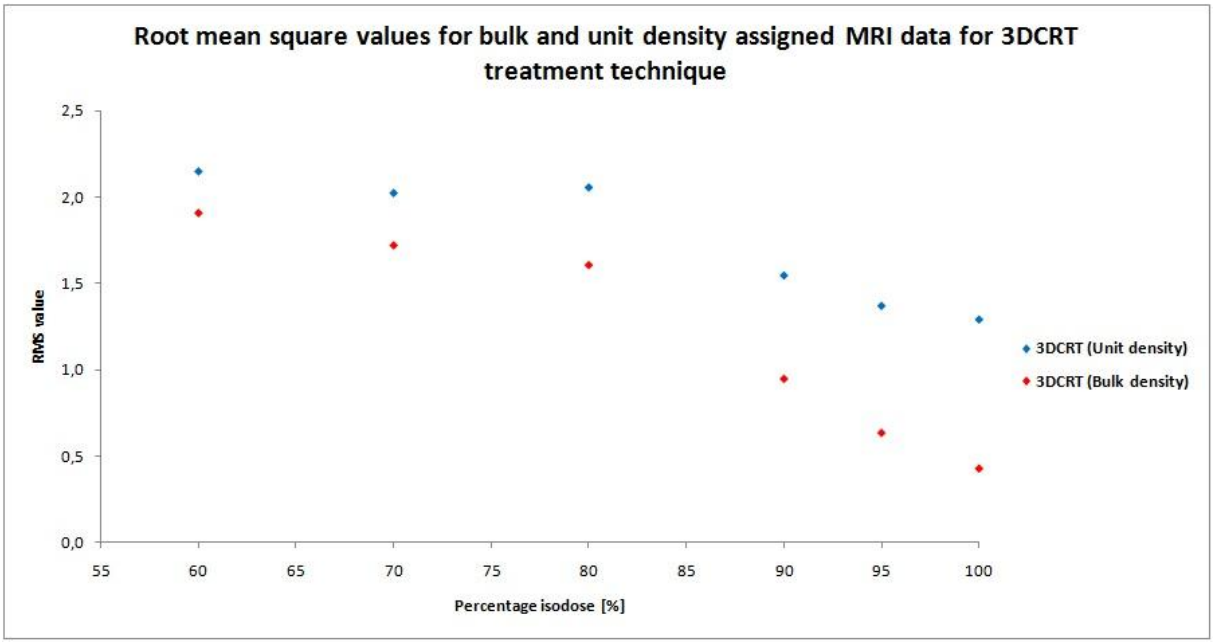

Figure 9. Mean rms values calculated for the 3DCRT treatment technique. Larger dose discrepancies can be found in the peripheral parts outside the target which leads to larger rms values when larger volumes are studied. It is also clear that MRI_{bones} is a better approximation than MRI_{water} for this treatment technique.

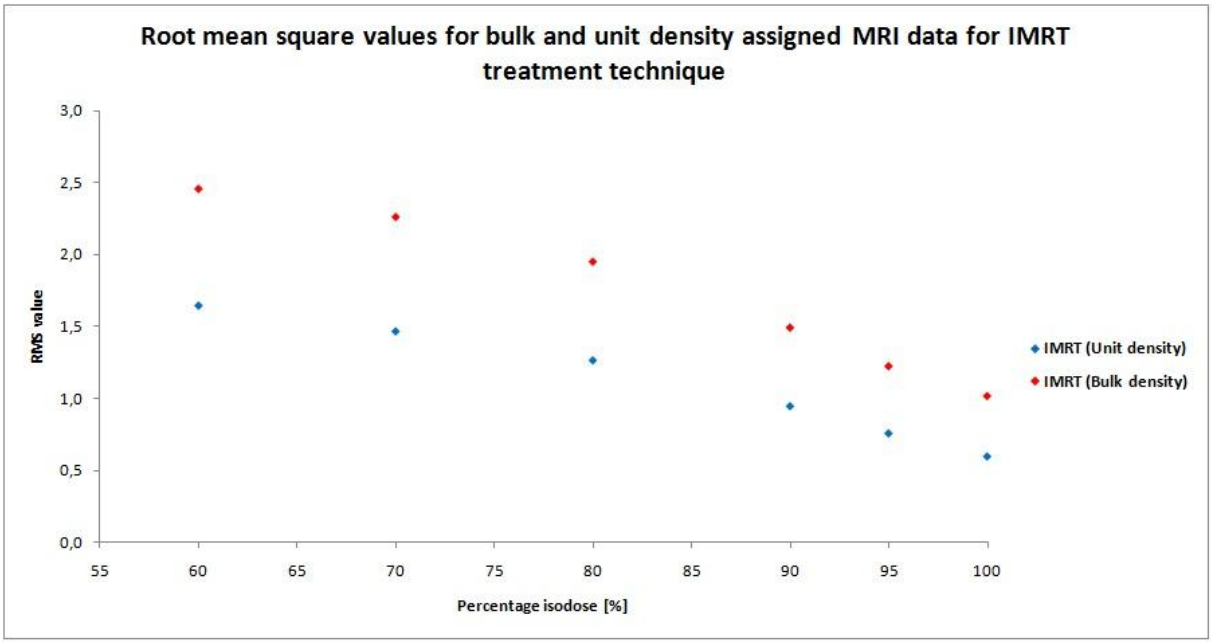

Figure 10. Mean rms values calculated for the IMRT treatment technique. The results show a clear advantage of MRI_{water} to MRI_{bones} for this treatment technique, which was unexpected considering the theoretical background.

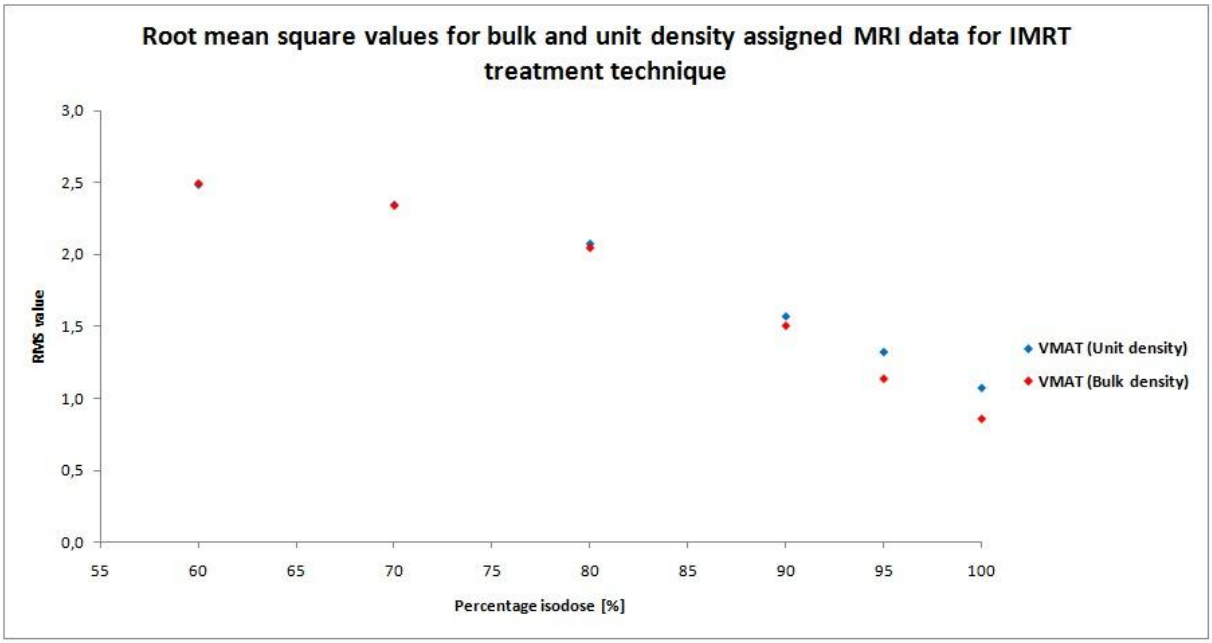

Figure 11. Mean rms values calculated for the VMAT treatment technique. The results are not as conclusive as those for 3DCRT and IMRT treatment techniques but a small advantage of MRI_{bones} over MRI_{water} can be seen.

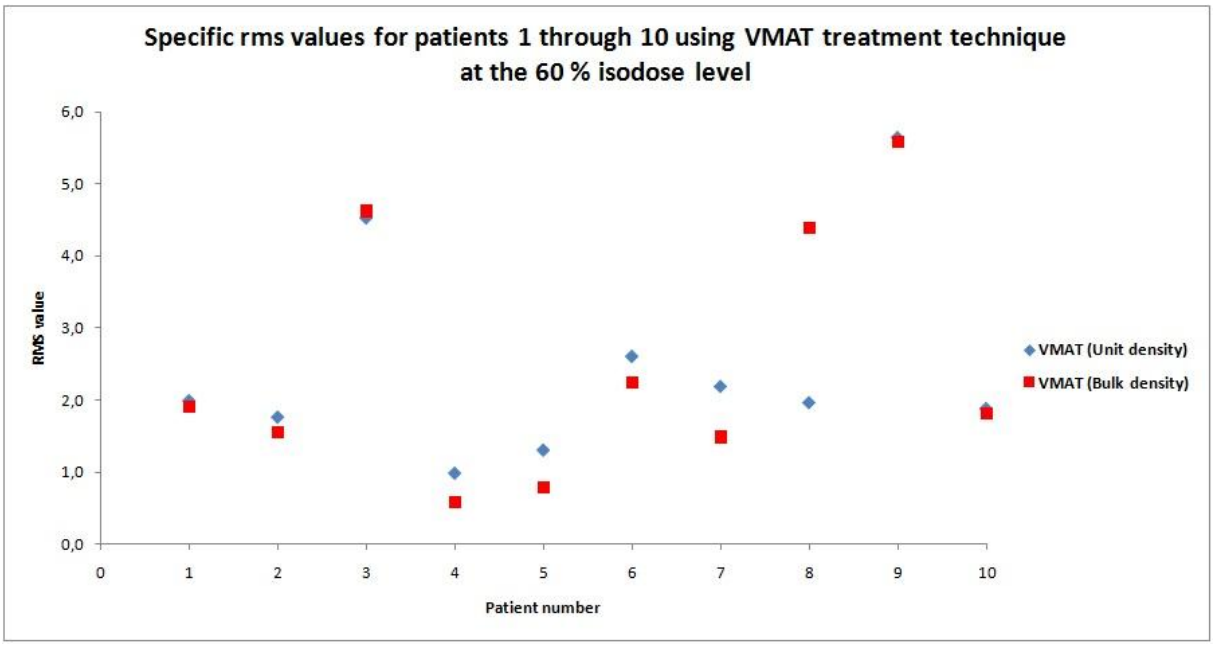

Figure 12. Rms values for the ten individuals patients for the volume enclosed by the 60 % isodose level. Patient #3 and #8 are anomalies in the sense that in these cases, MRI_{bones} is a worse approximation to CT than MRI_{water}. This treatment technique also shows the largest spread within the data.

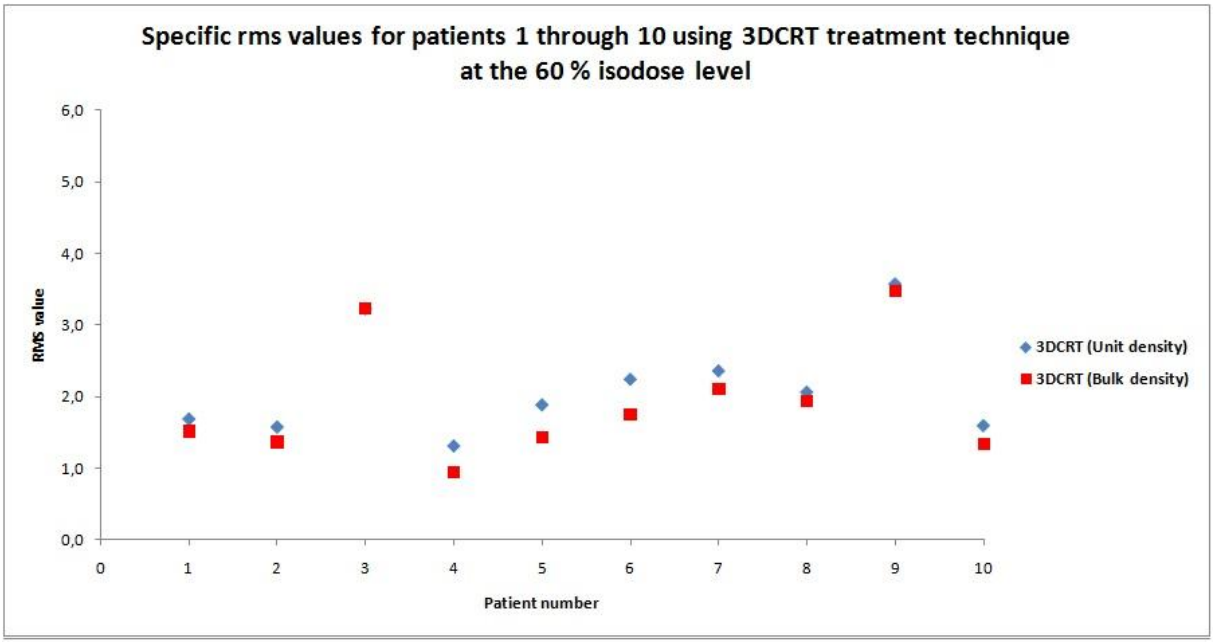

Figure 13. Rms values for the 3DCRT treatment technique for each individual patient in the volume enclosed by the 60 % isodose level. A consistent difference between the rms values calculated for MRI_{water} and MRI_{bones} can be seen, with exception for patient #3.

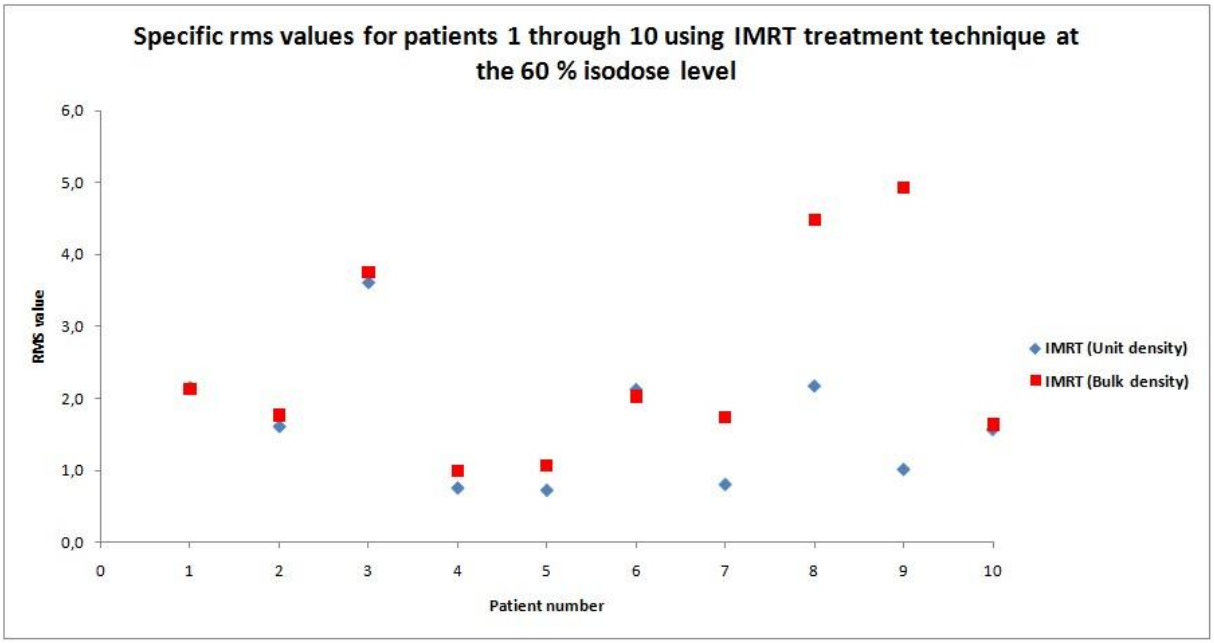

Figure 14. Rms values calculated for the individual patients using IMRT treatment technique in the volume enclosed by the 60 % isodose level. All rms values for the patients except patient #1 and #6 shows that MRI_{water} is a better approximation to CT.

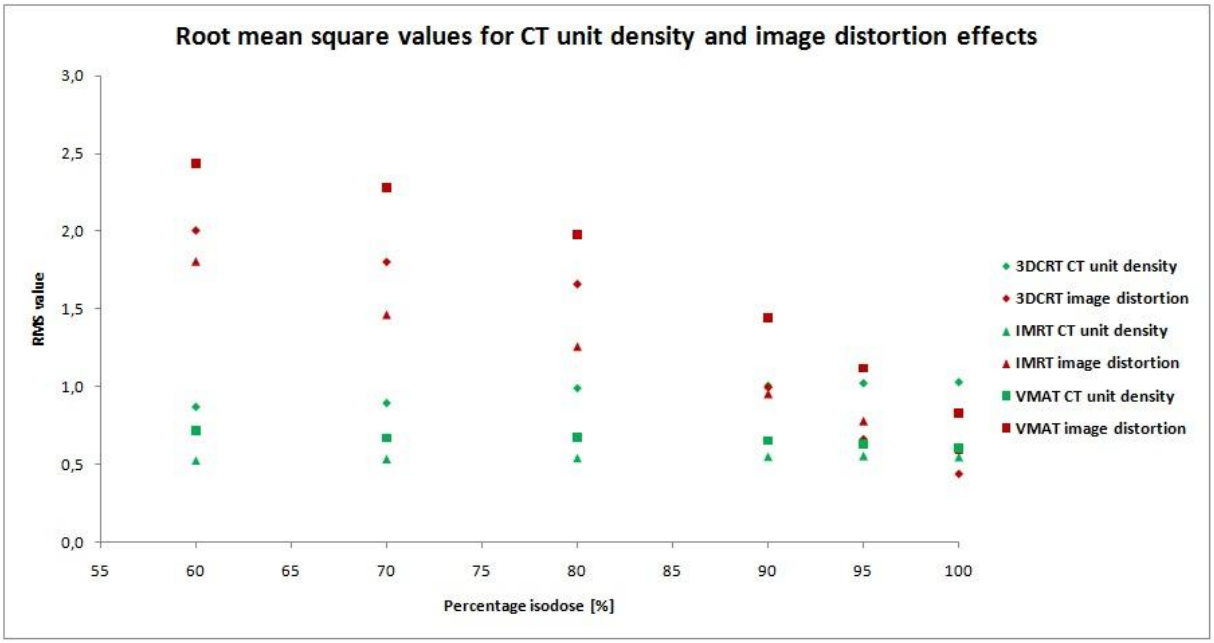

Figure 15. Mean rms values calculated for the three different treatment techniques comparing CT with CT_{water} ("CT unit density") and CT_{water} with MRI_{water} (" image distortion"). The inter-fractional differences together with the geometric distortion give the largest contribution to the dosimetric uncertainty and show a dependence of the volume size. Dose discrepancies arising from missing heterogeneity correction is invariant over the volume size.

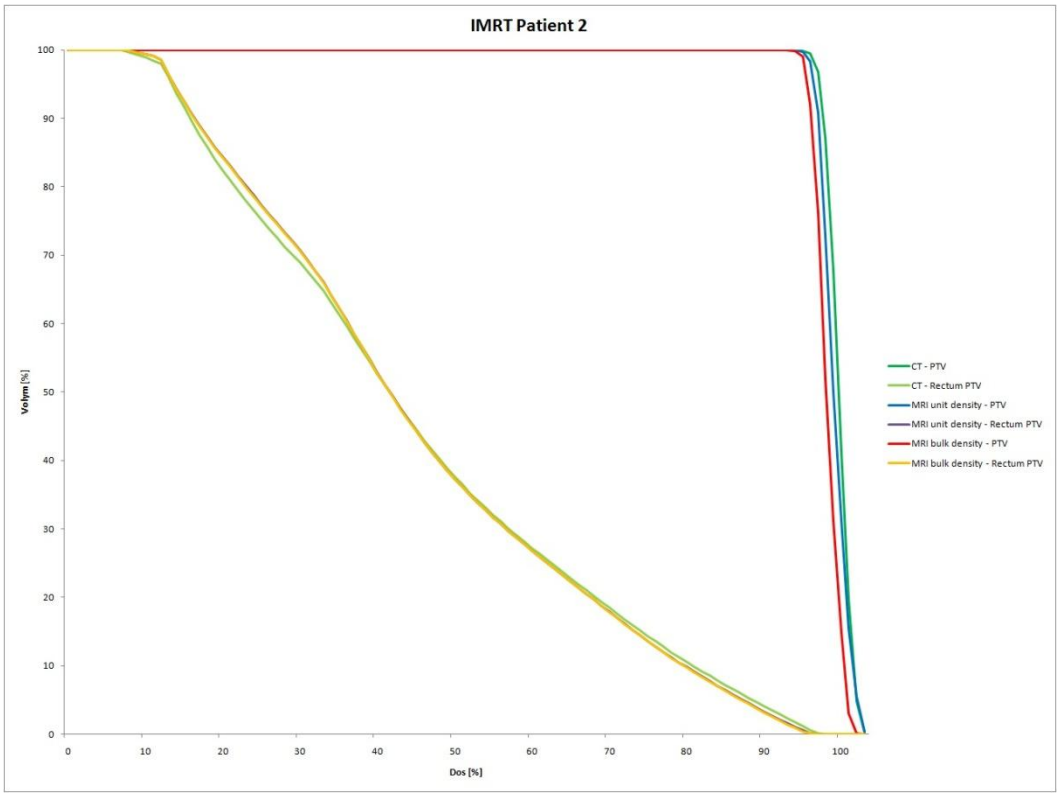

Figure 16. DVH for CT (Target green / OAR light green), MRI_{water} (Target blue / OAR purple) and MRI_{bones} (Target red / OAR yellow) for patient #2. The target is under dosed when calculating the plan on MRI_{bones} compared to the others.

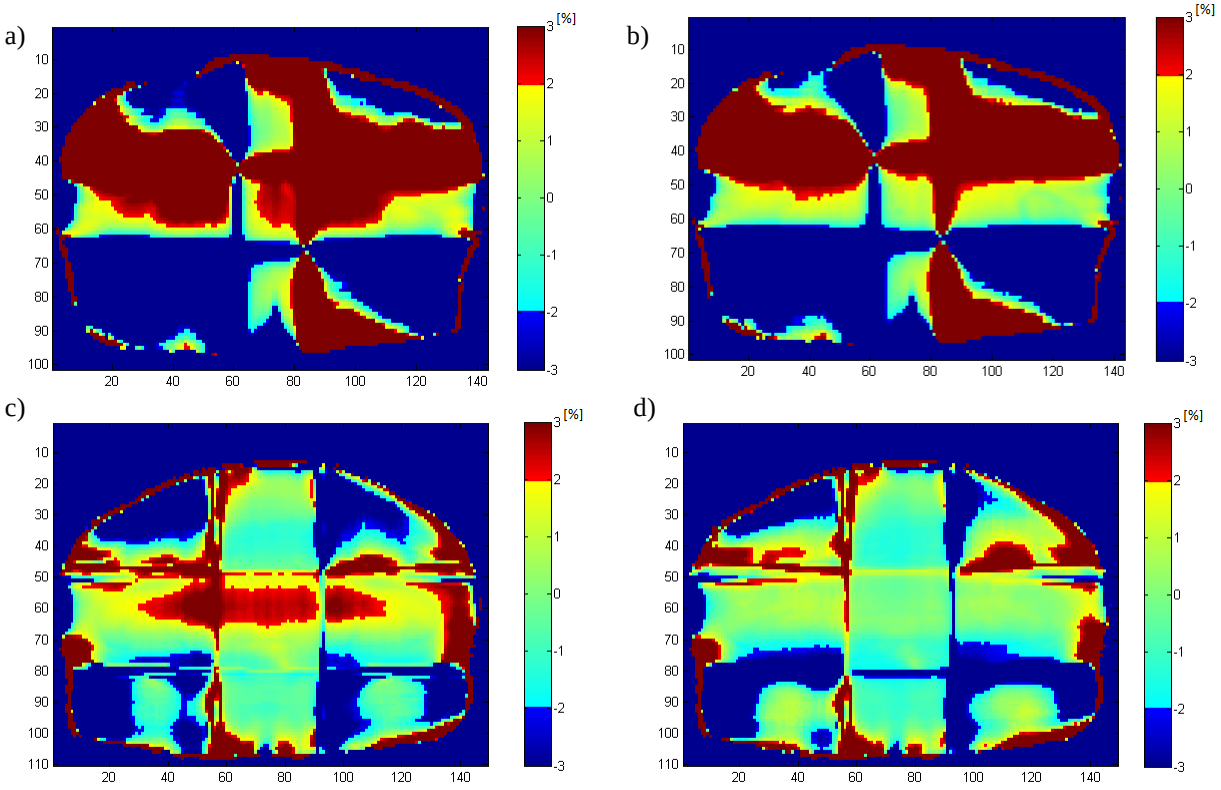

Figure 17. a) Percentage dose difference between CT and MRI_{water} for patient #3 showing a disagreement at the field edges and in clinically insignificant low-dose areas, b) Percentage dose difference between CT and MRI_{bones} for patient #3. A better agreement is found, especially inside the target in which a smaller volume is over dosed in comparison with the percentage dose distribution illustrated in figure 4, c) Percentage dose difference between CT and MRI_{water} for patient #4 where no spatial disagreement between the bulk of the dose distributions were found, resulting in lower percentage dose differences throughout the volume. An area inside the target shows a dose difference larger than 2 %, d) Percentage dose difference between CT and MRI_{bones} for patient #4. This illustration clearly shows an improvement of MRI_{bones} over MRI_{water}.

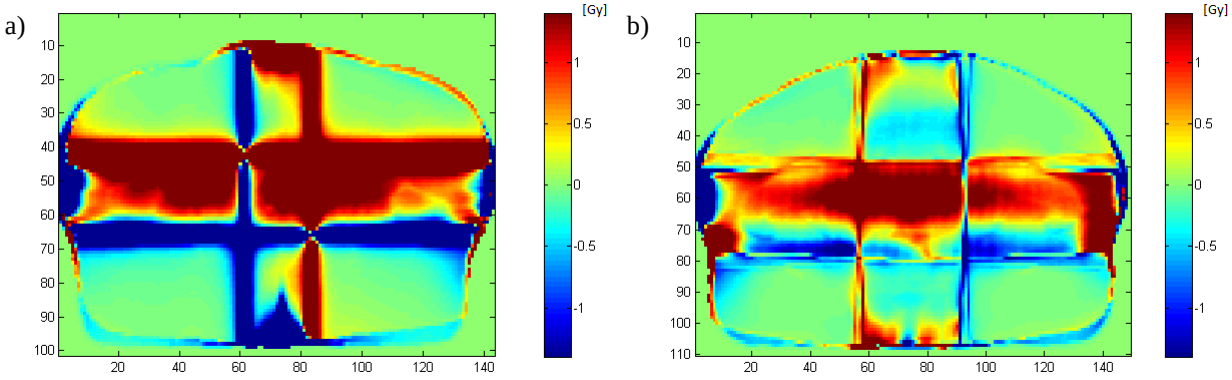

Figure 18. a) Absolute dose distribution for the same example as in figure 17a, b) Absolute dose distributions for the same example as in figure 17c.

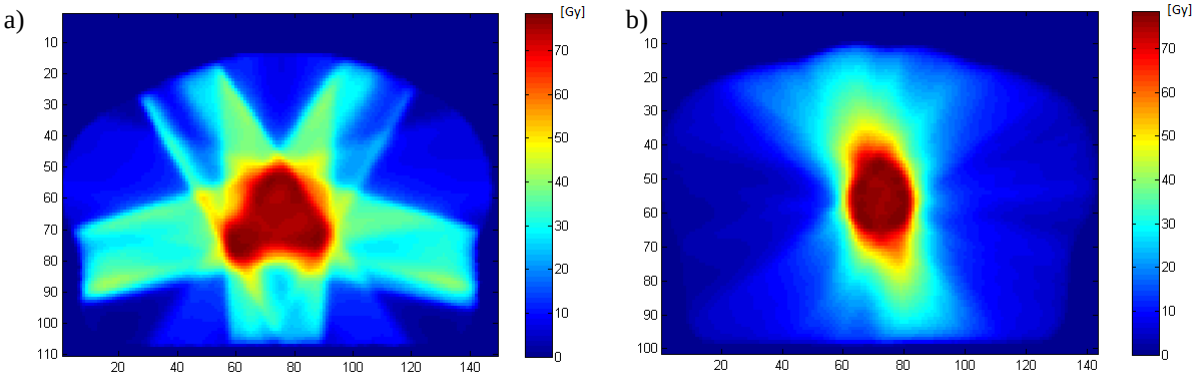

Figure 19. a) Absorbed dose distribution for an IMRT treatment of patient #3 calculated on CT, b) Absorbed dose distribution for a VMAT plan on CT for patient #3.

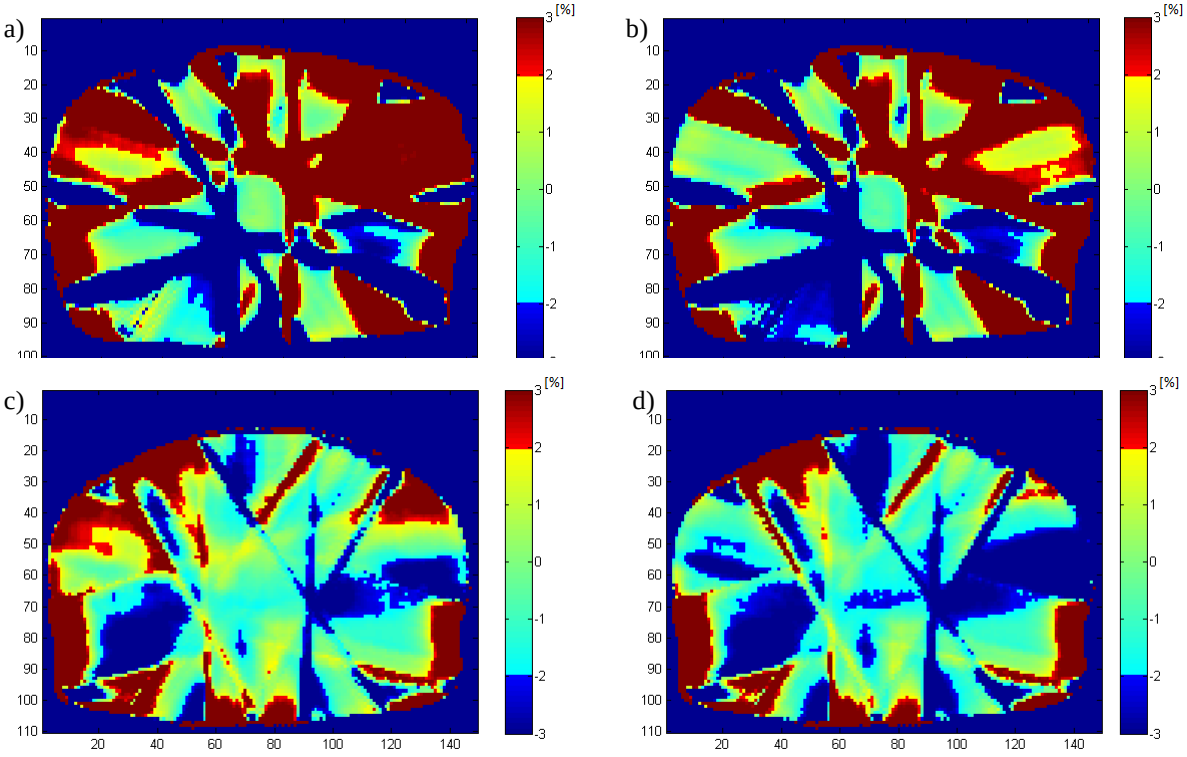

Figure 20. a) Percentage dose difference for patient #3 for the IMRT treatment technique between CT and MRI_{water}. Dose differences are prominent around the field edges and in low dose areas, b) Percentage dose distribution for the IMRT treatment technique for patient #3, using MRI_{bones}. Some areas show a better agreement with the dose distribution calculated for CT and some are worse, such as the area inside the target now tilting towards a light blue color tone instead of a greenish tone which indicates an under dosing of the target, c) Percentage dose difference for patient #4 for the IMRT treatment technique between CT and MRI_{water}, d) Percentage dose distribution for patient #4, using IMRT treatment technique and MRI_{bones}. When comparing to figure 10, this image shows greater under dosing in the target area, with values below -2 % in some parts of the target.

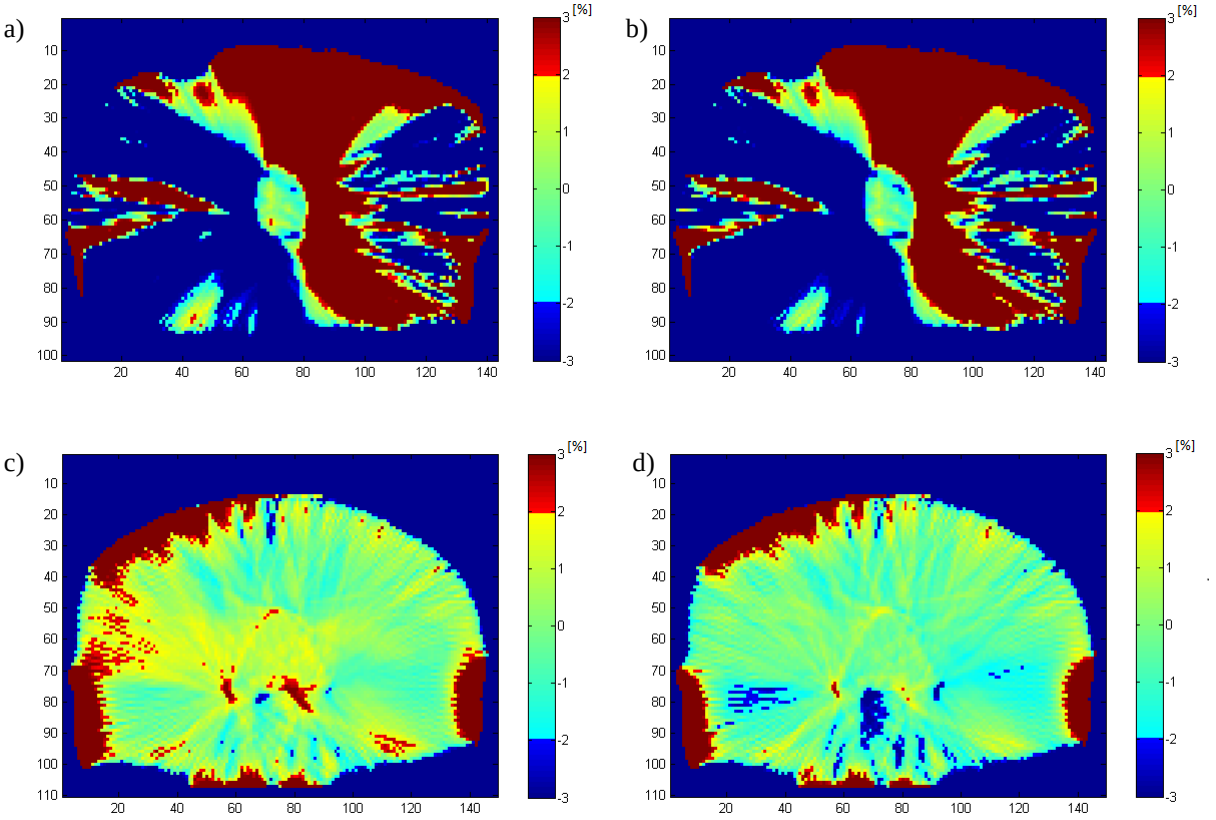

Figure 21. a) Percentage dose difference for patient #3 using VMAT treatment technique for MRI_{water}. Large areas with differences larger or equal than 3 % are present, b) Percentage dose difference for patient #3 using MRI_{bones}. When compared to the percentage dose difference in figure 14, no apparent difference can be found, c) Percentage dose difference for patient #4, using MRI_{water} on a VMAT treatment plan. There is generally a better agreement with the original dose distribution for patient #4 than for patient #3, d) Percentage dose difference for patient #4, now using MRI_{bones} for the VMAT treatment technique. An even better agreement with the original dose distribution is found than in the example with MRI_{water}.

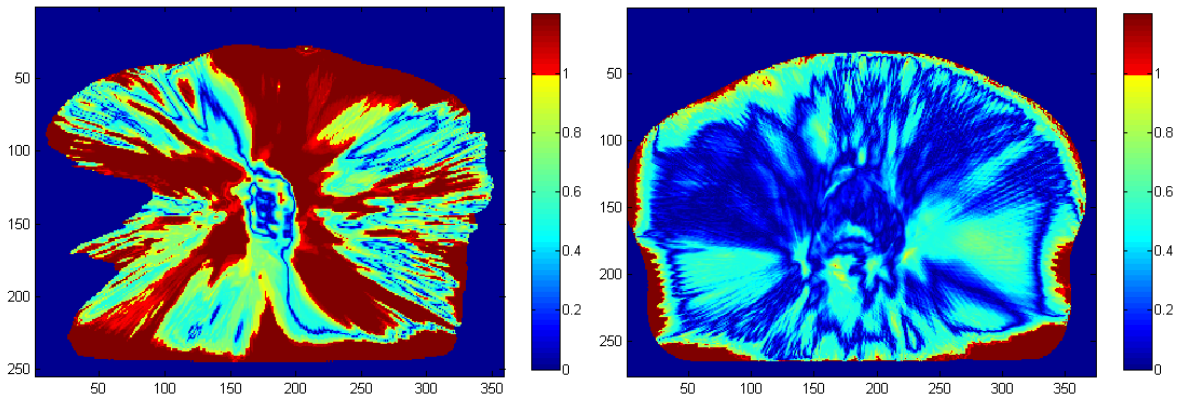

Figure 22. Example slices of the 3D gamma evaluation matrices for patient #3 (left) and patient #4 (right). It is clear that the agreement for patient #4 is better than that for patient #3, which fails the gamma test in clinically significant areas.

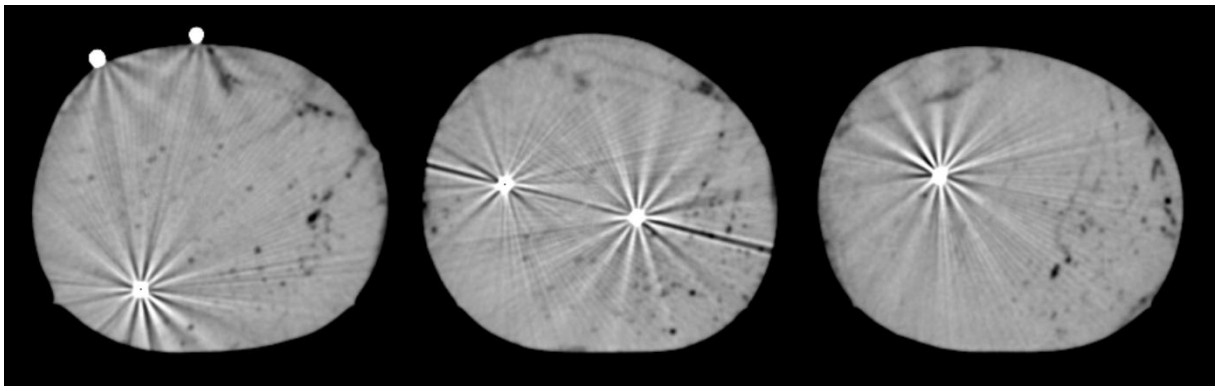

Figure 23. Images showing slices of the CT scan of the meat phantoms containing from left to right: 24 carat gold marker, 18 carat gold/copper markers and gold/iron marker. The markers give rise to prominent star artefacts as a result of the high attenuation properties of the metals combined with the filtered back-projection reconstruction algorithm.

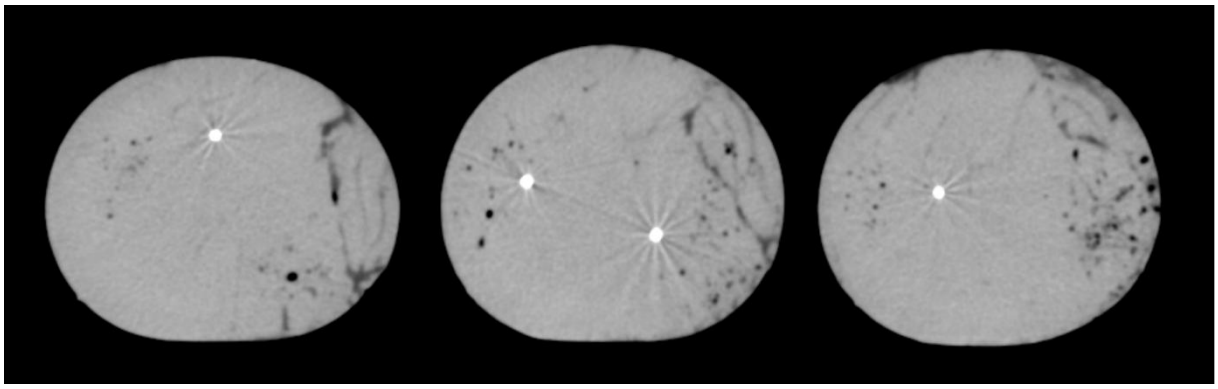

Figure 24. Images showing slices of the CT scan of the meat phantoms containing from left to right: gold/nitinol 1x3 mm marker, gold/nitinol 1.2x5 mm markers and carbon/zirconium marker. The markers are all clearly visible but do not give rise to star artefacts of any significant magnitude

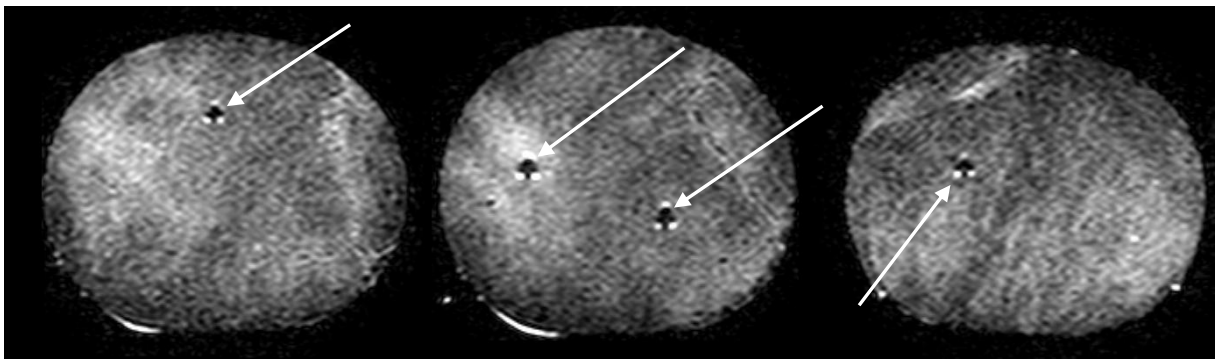

Figure 25. Images showing slices of the T2 weighted MRI scan of the meat phantoms showing from left to right: gold/nitinol 1x3 mm marker, gold/nitinol 1.2x5 mm markers and gold/iron marker.

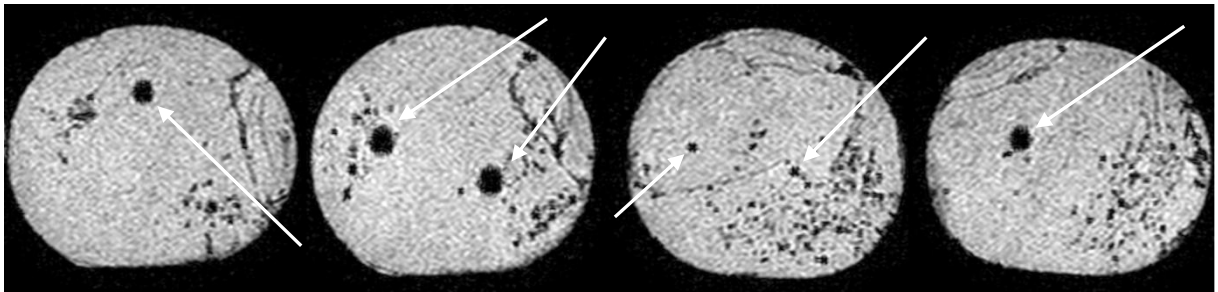

Figure 26. Images showing slices of the $T2^*$ weighted MRI scan of the meat phantoms showing from left to right: gold/nitinol 1x3 mm marker, gold/nitinol 1.2x5 mm markers, gold/copper markers and gold/iron marker.

The FFE sequence used to produce the images is a GRE based sequence, therefore more sensitive to magnetic susceptibility differences than the TSE which utilize a refocusing RF pulse.

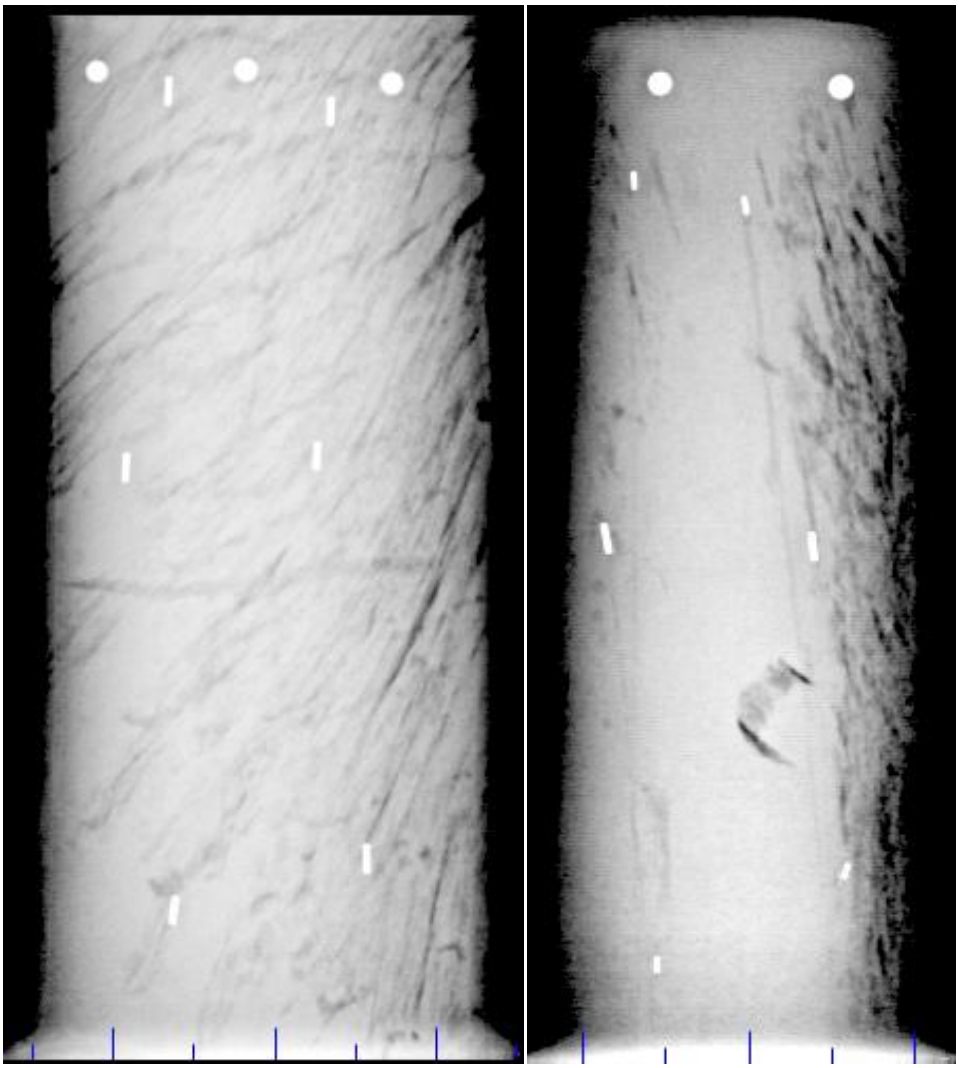

Figure 27. Images of the phantom obtained with the kV X-ray on-board imager system showing the classical gold implants (top left), copper/gold implant (middle left), gold/iron implants (bottom left), nitinol 1x3 mm implants (top right), nitinol 1,2 x 5 mm implants (middle right) and the carbon/zirkonium implants (bottom right).

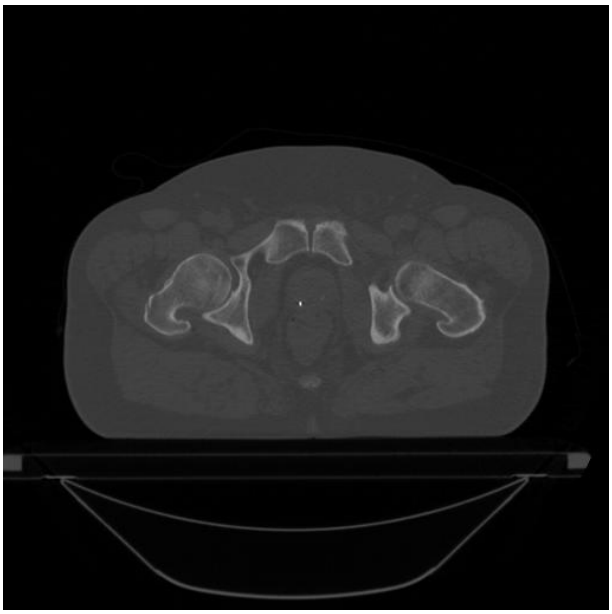

Figure 28. CT image of one of the volunteer patients showing the nitinol 1,2 x 5 mm implant in the prostate.

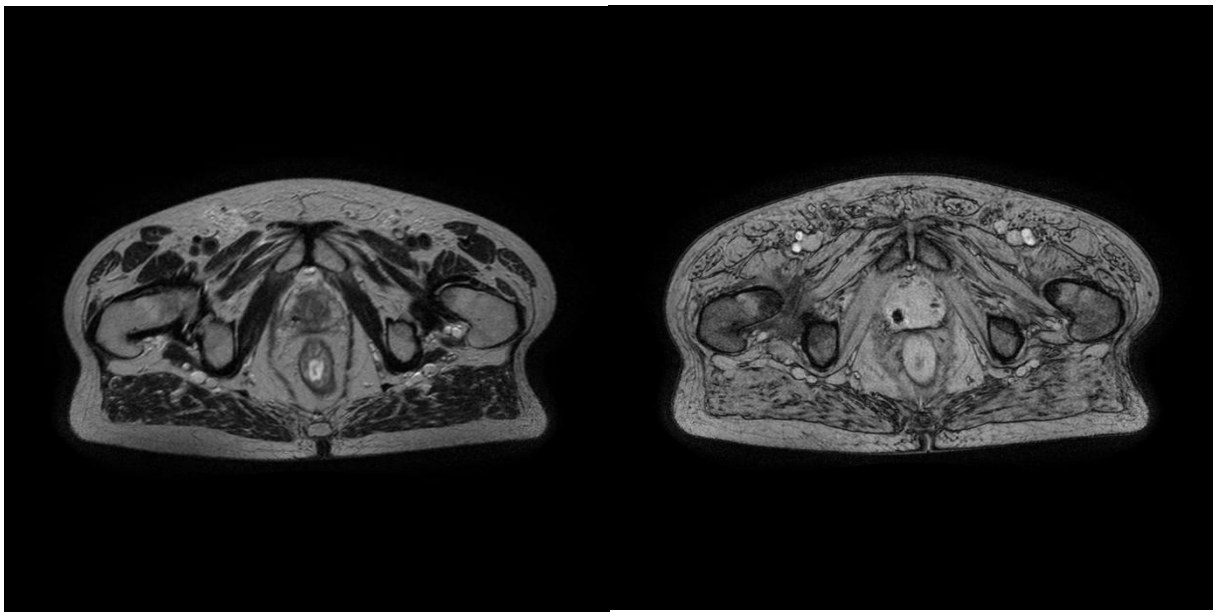

Figure 29. MRI images of the corresponding slice as in figure 40 showing the susceptibility artefact arising from the presence of the nitinol marker. T2W-TSE (left) and T2*W-TSE (right).

Appendix II - Abstract accepted at the ESTRO 29 conference

Dosimetric impact of performing dose calculations on bulk and unit density assigned MRI data for VMAT and IMRT treatments of prostate cancer

Authors: Johan Sjöberg[1,2], Brian Holch Kristensen[2] and David Sjöström[2]

[1]Medical radiation physics, Department of clinical sciences, Lund University, Lund, Sweden
[2]Copenhagen University hospital (Department of oncology), Herlev, Denmark

Topic: 19. Optimization and dose planning
Keywords: VMAT, IMRT, MRI

MRI provides better soft tissue contrast than CT and is an invaluable tool in the radiotherapy treatment process. The gold standard today is image fusion of MRI and CT data where targets and organs-at-risk are delineated on the MRI data and the dose calculations are performed on the CT data. It is appealing to exclude CT from the process in order to reduce cost and time and to eliminate the uncertainty inherited from the image fusion. Since MRI data does not contain any electron density information, this property must be assigned to the data. The purpose of this study is to evaluate the dosimetric consequences of performing dose calculations on unit density (water) and bulk density (water + bone) assigned MRI data for ten patients with prostate cancer using modern treatment techniques.

The patients were both MR- and CT-scanned. IMRT and Volumetric Modulated Arc Therapy (VMAT) plans were generated for the CT data, unit density assigned MRI data and bulk density assigned MRI data. The resulting dose distributions were compared by calculating the root-mean-square values (rms) for the volume enclosed by isodose levels 60%, 70%, 80%, 90%, 95% and 100% normalized to the prescription dose and by generating topographic maps of the percentage dose- and the absolute dose difference. DVH's were compared in order to study general tendencies in the dose distributions.

Dose differences <2% are observed within the target when bulk density was assigned for both VMAT and IMRT plans. Dose differences >2% are observed regardless of segmentation and treatment technique in low dose areas outside the target. A significant difference ($p<0.05$) is found between dose distributions calculated from unit density and bulk density assigned MRI data and between the different treatment techniques (see table). Higher rms values are acquired for larger volumes studied, which is attributable to larger dose discrepancies in low dose areas.

Assigning bulk densities in the patient reduces the dosimetric error resulting from ignoring tissue inhomogeneity to a clinically insignificant level, making MRI dose planning feasible. The reason why IMRT is more robust than VMAT for both unit density and bulk density assigned MRI data is that the fields in the IMRT plan are aligned to avoid bony areas in the pelvis while the VMAT field is not. The approximation of assigning densities is therefore more valid for the IMRT plans. However using avoidance sectors in the IMAT optimization procedure may improve the dosimetric accuracy if the field segments aligned through bony areas are excluded.

	IMRT unit density	IMRT bulk density	VMAT unit density	VMAT bulk density
60%	2.8 ± 1.3	2.4 ± 1.4	2.9 ± 1.2	2.0 ± 1.0
70%	2.4 ± 0.8	2.0 ± 0.8	2.8 ± 1.0	2.0 ± 0.9
80%	2.1 ± 0.5	1.6 ± 0.6	2.5 ± 0.6	1.7 ± 0.6
90%	1.8 ± 0.2	1.2 ± 0.3	2.0 ± 0.4	1.3 ± 0.4
95%	1.5 ± 0.2	0.9 ± 0.2	1.7 ± 0.4	1.0 ± 0.1
100%	1.3 ± 0.5	0.6 ± 0.2	1.4 ± 0.5	0.7 ± 0.2